Improved Geological Slip Rate Estimations in the Complex Alhama de Murcia Fault Zone (SE Iberia) and Its Implications for Fault Behavior

O Gómez-novell, M. Ortuño, J García-mayordomo, J M Insua-arévalo, T K Rockwell, S. Baize, J J Martínez-díaz, R. Pallàs, E. Masana

Tectonics

RESEARCH ARTICLE
10.1029/2022TC007465

Key Points:

- Multi-site paleoseismic surveys allow to improve the estimations of the geological slip rates in the Alhama de Murcia Fault (AMF)
- The AMF shows a geological slip rate between 1.35 and 1.64 mm/yr for the past 18–15 ka
- Late Quaternary slip rate fluctuations suggest strain rate variations and highlight possible synchronicities with neighboring faults

Supporting Information:

Supporting Information may be found in the online version of this article.

Correspondence to:

O. Gómez-Novell,
octavi.gomeznovell@unich.it;
octgomez@ub.edu

Citation:

Gómez-Novell, O., Ortuño, M., García-Mayordomo, J., Insua-Arévalo, J. M., Rockwell, T. K., Baize, S., et al. (2022). Improved geological slip rate estimations in the complex Alhama de Murcia Fault zone (SE Iberia) and its implications for fault behavior. *Tectonics*, *41*, e2022TC007465. https://doi.org/10.1029/2022TC007465

Received 21 JUN 2022
Accepted 3 DEC 2022

Author Contributions:

Conceptualization: O. Gómez-Novell, M. Ortuño, J. García-Mayordomo, E. Masana
Funding acquisition: R. Pallàs, E. Masana
Investigation: O. Gómez-Novell, M. Ortuño, J. García-Mayordomo, J. M. Insua-Arévalo, T. K. Rockwell, S. Baize, J. J. Martínez-Díaz, R. Pallàs, E. Masana
Methodology: O. Gómez-Novell, M. Ortuño, J. García-Mayordomo, J. M.

Improved Geological Slip Rate Estimations in the Complex Alhama de Murcia Fault Zone (SE Iberia) and Its Implications for Fault Behavior

O. Gómez-Novell[1,2], M. Ortuño[1], J. García-Mayordomo[3], J. M. Insua-Arévalo[4], T. K. Rockwell[5], S. Baize[6], J. J. Martínez-Díaz[4], R. Pallàs[1], and E. Masana[1]

[1]Departament de Dinàmica de la Terra i l'Oceà, Universitat de Barcelona, Barcelona, Spain, [2]Dipartimento INGEO, Università degli Studi "Gabriele d'Annunzio" Chieti-Pescara, Chieti, Italy, [3]Instituto Geológico y Minero de España – CSIC, Madrid, Spain, [4]Departamento de Geodinámica, Universidad Complutense de Madrid, Madrid, Spain, [5]Department of Geological Sciences, San Diego State University, San Diego, CA, USA, [6]Institut de Radioprotection et Sûreté Nucléaire, Fontenay-aux-Roses, France

Abstract Fault slip rate is one of the most crucial parameters to characterize earthquake occurrence in fault-based seismic hazard assessments (SHA). Accordingly, paleoseismic studies have increasingly focused on constraining this parameter in active faults worldwide. We present a comprehensive paleoseismic study in the Alhama de Murcia Fault (AMF), one of the most active faults in SE Spain and source of destructing earthquakes such as the 2011 M_w 5.2 Lorca event. Contrasting with previous studies, we integrate paleoseismic data from four fault strands in the AMF and, based on trench slip analysis and numerical dates, we derive slip rate estimates of each strand over the whole transect and assess their time variability. The AMF has a minimum net slip rate between $1.35^{+0.16}/_{-0.10}$ and $1.64^{+0.16}/_{-0.11}$ mm/yr for the past 18 ± 1 to 15.2 ± 1.1 ka. These results prove the importance of accounting for the complete sections of a geological structure as they are almost twice the previous estimates for a single fault branch. Slip rate variability is identified in the AMF, with cyclic acceleration-quiescence patterns that could be related to stress field changes driven by fault interaction or synchronicity with neighboring faults (e.g., Carrascoy). We hope that the data presented here motivates their inclusion into forthcoming fault-based SHAs. In this regard, limitations related to the lack of paleoseismic data for one fault strand, along with poor characterization of the strike component of slip and insufficient age control of the units for another strand are highlighted and need to be accounted for by modelers.

1. Introduction

Characterizing the fault slip rate is one of the most important steps in active tectonics research because it is a critical parameter to infer earthquake rates in fault-based probabilistic hazard assessments (e.g., Field et al., 2015; Gómez-Novell et al., 2020; Stirling et al., 2012; Valentini et al., 2017; Woessner et al., 2015). The estimation of this parameter in low to moderate strain regions is usually challenging because the rates of surface processes that shape landscapes might overcome and/or mask the expression of tectonic deformation at/near the surface, especially if the deformation is diffuse and distributed over wide and complex fault zones. For these reasons and in these settings, a reliable fault characterization based on geomorphological, paleoseismic, and geodetic studies requires additional efforts, observation sites along fault strands and lengthier geodetic records.

A common practice in paleoseismology (due to lack of resources) is to assume fault characterization observations from a unique location as representative of the entire length of a fault. This issue is further emphasized when applied to distributed deformation areas where observations are scarcer and, for this reason, the integration of data from multiple sites is usually the most reliable way to improve the representation of fault parameters. Supporting this reasoning, multi-site paleoseismic data allowed the scientific community to improve the understanding of faults as structures able to accommodate deformation in complex slip patterns, by sometimes simultaneously rupturing and interacting (e.g., Dolan et al., 2007; DuRoss et al., 2011, 2021; Ren et al., 2013). Here, we apply this multi-site concept in the framework of SE Spain.

The SE of Spain is one of the most seismically active regions of Iberia and has accommodated some of its largest earthquakes during historical times (I_{EMS} = VIII–IX): 1522 Almería, 1674 Lorca, 1804 Dalías-Berja or 1829 Torrevieja events (Martínez Solares, 2003; Mezcua, 1982; Silva et al., 2014) (Figure 1a). This list includes the

Insua-Arévalo, T. K. Rockwell, S. Baize, J. J. Martínez-Díaz, R. Pallàs, E. Masana
Supervision: O. Gómez-Novell, M. Ortuño, J. García-Mayordomo, J. M. Insua-Arévalo, T. K. Rockwell, S. Baize, J. J. Martínez-Díaz, E. Masana
Validation: O. Gómez-Novell, M. Ortuño, J. García-Mayordomo, J. M. Insua-Arévalo, T. K. Rockwell, S. Baize, J. J. Martínez-Díaz, E. Masana
Visualization: O. Gómez-Novell
Writing – original draft: O. Gómez-Novell
Writing – review & editing: O. Gómez-Novell, M. Ortuño, J. García-Mayordomo, J. M. Insua-Arévalo, T. K. Rockwell, S. Baize, J. J. Martínez-Díaz, R. Pallàs, E. Masana

2011 M_w 5.2 Lorca earthquake (Alguacil et al., 2014; López-Comino et al., 2012) that stands out as the largest and most damaging event of the past 50 years. Such context has motivated several paleoseismic and geodetic studies over the past decades, focused on characterizing the SE Iberian faults' slip rates and quantifying the main parameters needed for the seismic hazard assessments (SHA) (e.g., Echeverria et al., 2013, 2015; Insua-Arévalo et al., 2015; Martín-Banda et al., 2015, 2021; Martínez-Díaz et al., 2003; Masana et al., 2004, 2005, 2018). Most of these faults are part of the Eastern Betics Shear Zone (EBSZ), one of the main active fault systems in Spain.

In general, the EBSZ faults encompass a broad, distributed deformation zone with several active fault branches. Nonetheless and with some exceptions (e.g., Ortuño et al., 2012), the majority of paleoseismic studies there have been restricted to single sites along single fault strands due to the limited availability of recent Quaternary sediments (e.g., Ferrater et al., 2016) and erosion predominance (Silva et al., 2003), especially in proximal parts of the mountain ranges. This fact implies that the paleoseismic parameters estimated for these faults, and notably their slip rates, are potentially underestimated and underrepresented. Therefore, characterizing all structures within the whole system is necessary.

Herein, we present a comprehensive paleoseismic study on one of the most active faults of the EBSZ, the Alhama de Murcia Fault (AMF), by means of paleoseismic surveys along four sub-parallel fault branches that represent a transect across the entire fault zone. Our aim is to improve the overall quality of AMF slip rate estimates by integrating paleoseismic data from multiple sites. We also analyze the slip rate variability over time to detect possible patterns and discuss their causes and implications for seismic hazard. To do so, we perform (a) a detailed field geomorphological and structural characterization, (b) an exhaustive fault slip analysis in each of the trenched locations and (c) numerical dating of the sediments using radiocarbon and Optically Stimulated Luminescence (OSL) techniques.

2. The Alhama de Murcia Fault

The AMF is a ~87 km long reverse-strike slip fault located in the central part of the EBSZ, a ~400 km long transpressive tectonic corridor (Bousquet, 1979; Martínez-Díaz, 1998; Montenat, 1973; Silva et al., 1993) that accommodates an important part of the convergence between Africa and Eurasia (4–6 mm/yr; e.g., DeMets et al., 2015). The AMF is one of the most active and prominent structures of the EBSZ (Martínez-Díaz, 1998; Masana et al., 2004; Silva et al., 1992) with a marked geomorphological expression, paleoseismic evidence, and historical and instrumental seismicity (Figure 1a). According to Martínez-Díaz et al. (2018), at least eight I_{EMS} > VI earthquakes have occurred within <10 km of the AMF since the 16th century (e.g., 1674 I_{EMS} VIII, 1818 I_{EMS} VI–VII and 1579 I_{EMS} VII events in Lorca, and the 1908 and 1910 I_{EMS} VI events in Alcantarilla; Figure 1b). More recently, the AMF has produced several moderate magnitude earthquakes, with the 2011 M_w 5.2 Lorca earthquake (Alguacil et al., 2014; López-Comino et al., 2012) standing out for its impact: 9 deaths, extensive damage across the city of Lorca and losses over 1200 million euros (Martínez-Díaz, Masana, & Ortuño, 2012).

The AMF constitutes the NW tectonic limit between the Guadalentín Depression and the uplifted ranges (Las Estancias, La Tercia, Espuña; Figure 1c) with Paleozoic-Cenozoic basement. Along these ranges and to their SE, the AMF displaces several generations of Quaternary alluvial fans (Figure 2a) (e.g., Martínez-Díaz, 1998; Silva et al., 1992). Based on its geomorphological expression, fault orientation and seismicity, the AMF is divided into four along-strike segments (Martínez-Díaz, Masana, & Ortuño, 2012; Silva, 1994), with the two SW segments being the ones with stronger (more recent and higher cumulative displacement) geological evidence of activity (Góñar-Lorca and Lorca-Totana; Figure 1c). Thus, the majority of geomorphic, paleoseismic and geodetic studies in the AMF have focused on these two segments (e.g., Echeverria et al., 2013; Ferrater et al., 2016, 2017; Martínez-Díaz et al., 2003; Masana et al., 2004; Ortuño et al., 2012), and particularly in the central Lorca-Totana segment.

To date, the paleoseismic slip rate of the Lorca-Totana segment is estimated to be 0.9 ± 0.1 mm/yr for the past 22.1 ± 0.2 to 15.2 ± 1.1 ka (Ferrater et al., 2016), and agrees with the geomorphic rate of 1.0 ± 0.2 mm/yr for the past 30 ka (Ferrater et al., 2017). These rates are also consistent with the geodetic left-lateral rate of 1.5 ± 0.3 mm/yr across the whole Guadalentín Depression (Echeverria et al., 2013), which suggest a control of the AMF in the structural development of the basin in this area (Ferrater et al., 2016). The current geological slip rate estimates, however, were obtained from a single site along one fault branch (Ferrater et al., 2016 at El Saltador site; Figures 2 and 3) out of the three proposed Lorca-Totana fault strands (Ferrater et al., 2017). In the

10.1029/2022TC007465

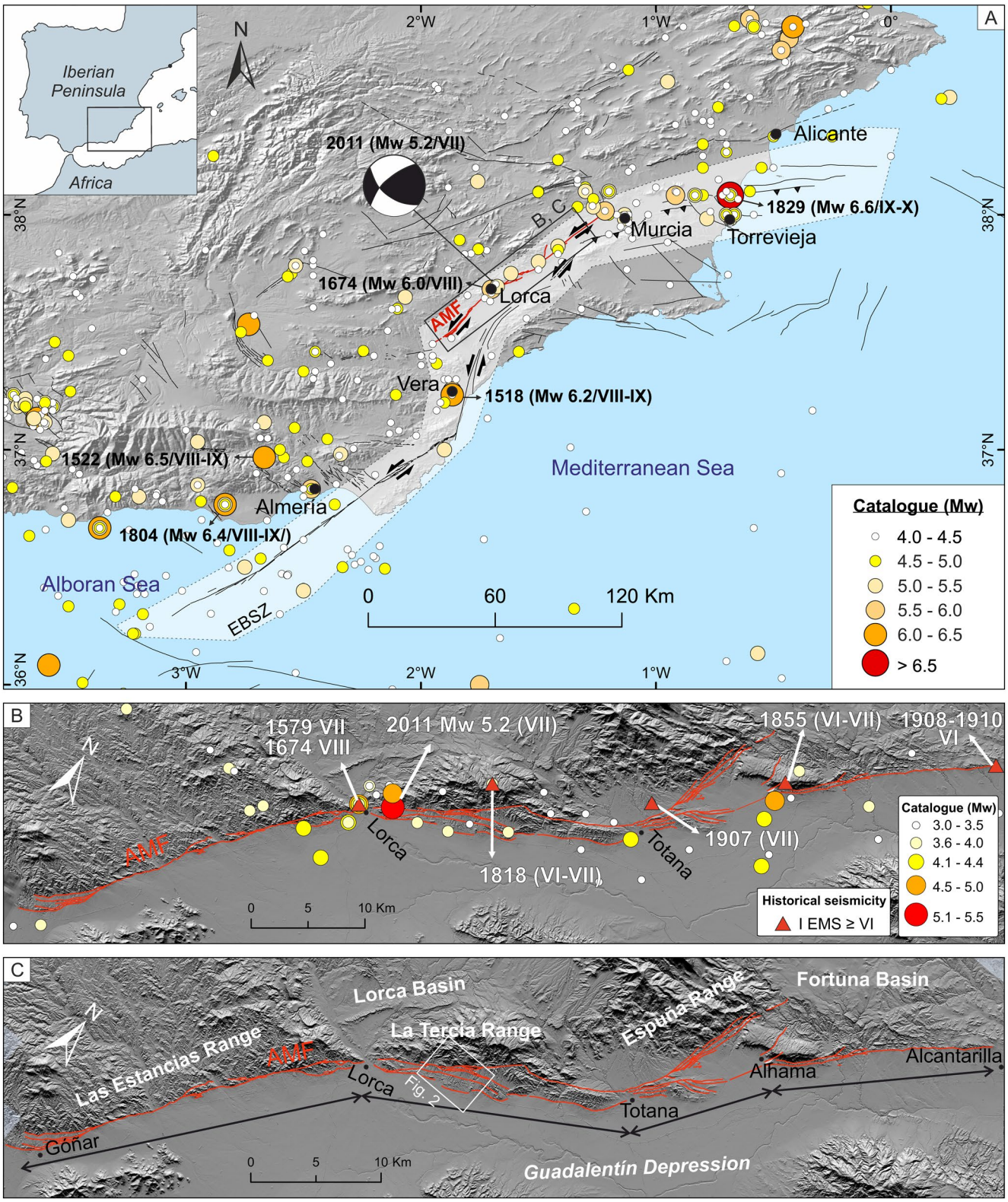

Figure 1.

present study, following the thesis work by Gómez-Novell (2021), we recognize and describe two additional fault strands along this segment, increasing the count up to a total of five. To completely characterize the entire fault-system slip rate, paleoseismic information is needed for all branches. Thus, such an information gap is the impetus for the development of our study.

3. Methods

A trenching analysis is performed to infer the geological slip rates of the AMF. To do so, we carried out geomorphological and structural mapping in the Lorca-Totana segment (Figure 2), and a paleoseismic investigation from eight paleoseismic trenches at four sites across four fault strands (out of five) in a NW–SE transect of the AMF (Figure 2a). From NW to SE, the sites are referred to as La Tercia (T-2, T-6), El Roser (T-1), El Saltador (T-16) and La Hoya (T-0, T-3, T-4, T-5). At the El Saltador site, T-16 is an enlargement of a previous trench (TR-7; Ferrater et al., 2016) (Figures 3d and 3e). At the La Hoya site, only T-3 provides useful paleoseismic data for the purpose of this study.

To quantify the deformation, a vertical throw analysis is carried out from trench observations where uplift related to folding is detected (Figure S1 in Supporting Information S1), and a paleochannel lateral offset analysis is carried out in the trenches with strike slip component. The final throw and slip values result from several measurements per horizon, and are expressed as the mean and corresponding uncertainties (1σ interval).

The age of the deformation is established by dating a total of 19 new samples throughout the stratigraphy: 10 with OSL and 9 with radiocarbon. We also use 6 OSL dates from a previous trenching survey at the El Saltador site (Ferrater, 2016) (see results in Section 5.2):

For the OSL dates, fine-grained alluvial sediments are sampled in all cases using opaque aluminum cylindric tubes (20 × 4 cm), properly sealed with duct tape and kept from light exposure. Based on the information provided by the respective laboratories, the absorbed dose measurements are conducted using 90–250 μm quartz multi-grain aliquots (the number of aliquots read per sample varied from a minimum of 24 to a maximum of 72) and following the SAR-OSL protocol (e.g., Murray & Wintle, 2000, 2003) with Risø readers DA-20. Dose rate measurements are obtained after determining the moisture of each sample, concentration of U, Th, and K isotopes, and in situ gamma spectrometry carried out by the staff of each laboratory. The statistical model used to calculate luminescence ages is the Central Age Model (CAM; Galbraith & Roberts, 2012) for the samples of T-1, T-2, T-6, and T-16, while the Robust Mean (RM; AMC, 2001) for T-3 (see Table 1). In all cases outliers are excluded. Dates are provided in calendar years, which we transform to years before present (BP).

For the radiocarbon dates, fossil snail shell fragments (1–2 cm diameter) and charcoal fragments (1–5 mm diameter) are sampled from the sediments in the trenches with a spatula, wrapped into aluminum foil and stored into suitable airtight plastic bags. Based on the information provided by the respective laboratories, radiocarbon concentrations (fraction of modern), radiocarbon age and correction for isotopic fractionation are carried out following Stuiver and Polach (1977). Measurements are conducted on an AMS spectrometer. We calibrate the dates to years BP using the OxCal v.4.3.2 software (Ramsey, 2017) and the IntCal20 atmospheric curve (Reimer et al., 2020).

Finally, slip rates are computed combining the measured slips and numerical dates. For a better assessment of the uncertainties we use the MATLAB code by Zechar and Frankel (2009). Detailed methods for the deformation quantification, sampling, dating procedures in each laboratory and trenching survey are available in the Supporting Information S1 of this paper. Uninterpreted trench images and MATLAB scripts are available in an online repository (Gómez-Novell et al., 2022; see Open Research statement) to reproduce the slip measurements and slip rate calculations presented in this work.

Figure 1. (a) Seismotectonic setting of SE Iberia with the traces of the main active faults (QAFI database v4; IGME, 2022) and the 1048–2011 seismicity ($M_w \geq 4.0$; IGN-UPM, 2013). The buffer area of the Eastern Betic Shear Zone (ZESIS database; IGME, 2015) is drawn around the faults, and the most damaging historical and instrumental earthquakes are highlighted, including the 2011 M_w 5.2 Lorca earthquake (focal mechanism extracted from IGN, 2011). Intensity scale is European Macroseismic Scale (EMS98). Hillshaded relief from the WMS service by IGN (https://servicios.idee.es/wmts/mdt) (b) Instrumental ($M_w \geq 4.0$) and historical (IEMS ≥ VI) seismicity around the Alhama de Murcia Fault (AMF). Main earthquakes are indicated by arrows. (c) Main geological features and segmentation of the AMF. Hillshaded relief obtained from the LiDAR-based 2 m DTM by the IGN agency (MDT02; https://centrodedescargas.cnig.es).

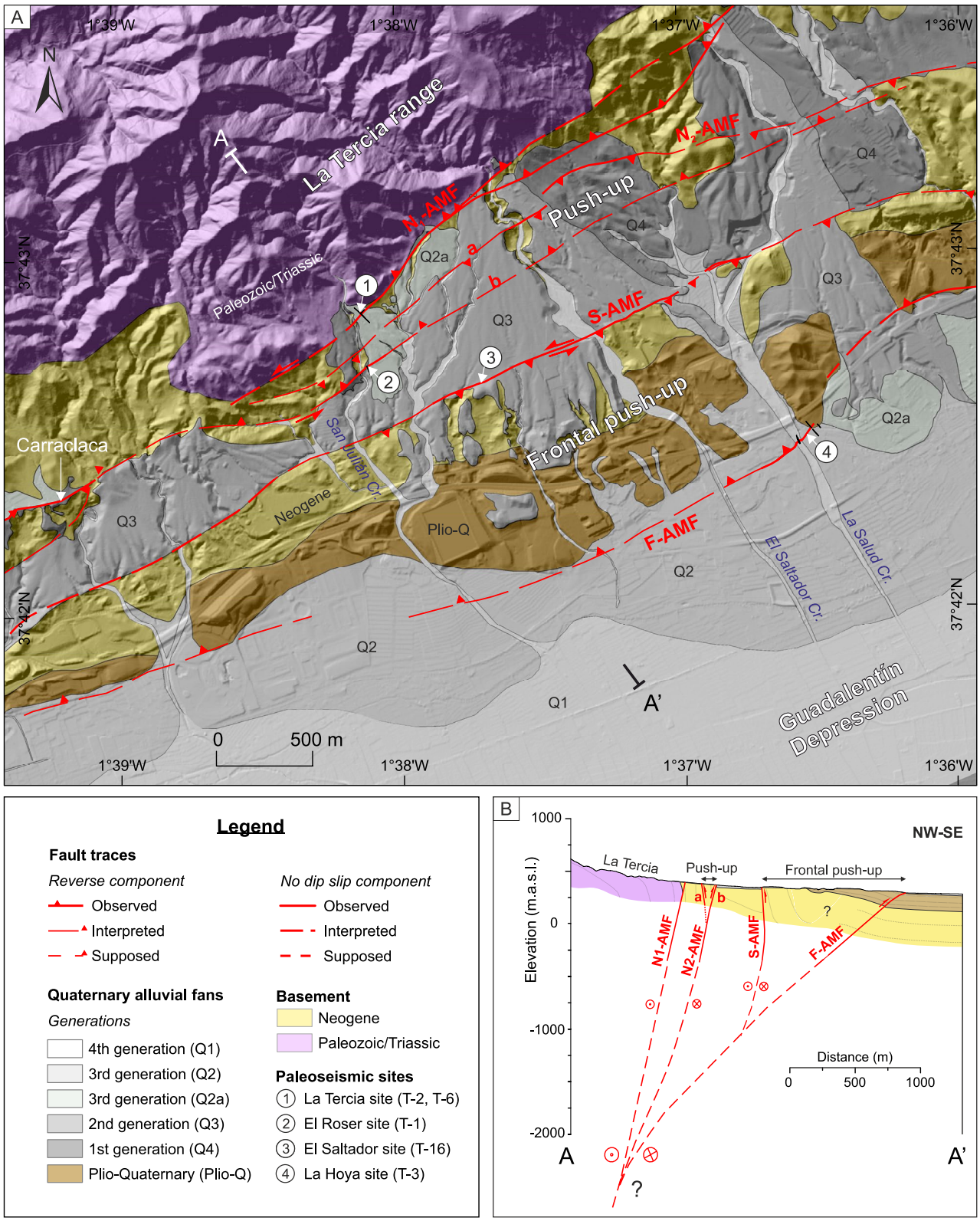

Figure 2. (a) Geological map of the studied area within the Lorca-Totana segment of Alhama de Murcia Fault (AMF). The numbers in circles indicate the location of the different paleoseismic sites from NW to SE, which can be viewed in the images of Figure 3. The location of the A-A' cross section is also indicated. Hillshaded relief obtained from the LiDAR-based 2 m DTM by the IGN agency (MDT02; https://centrodedescargas.cnig.es) and basement cartography is based on the Spanish Geological Map (1:50,000) zone 2100 (Marín-Lechado et al., 2011). (b) Geological cross section of the studied transect with our proposal of deep structure for the AMF, based exclusively on surface data.

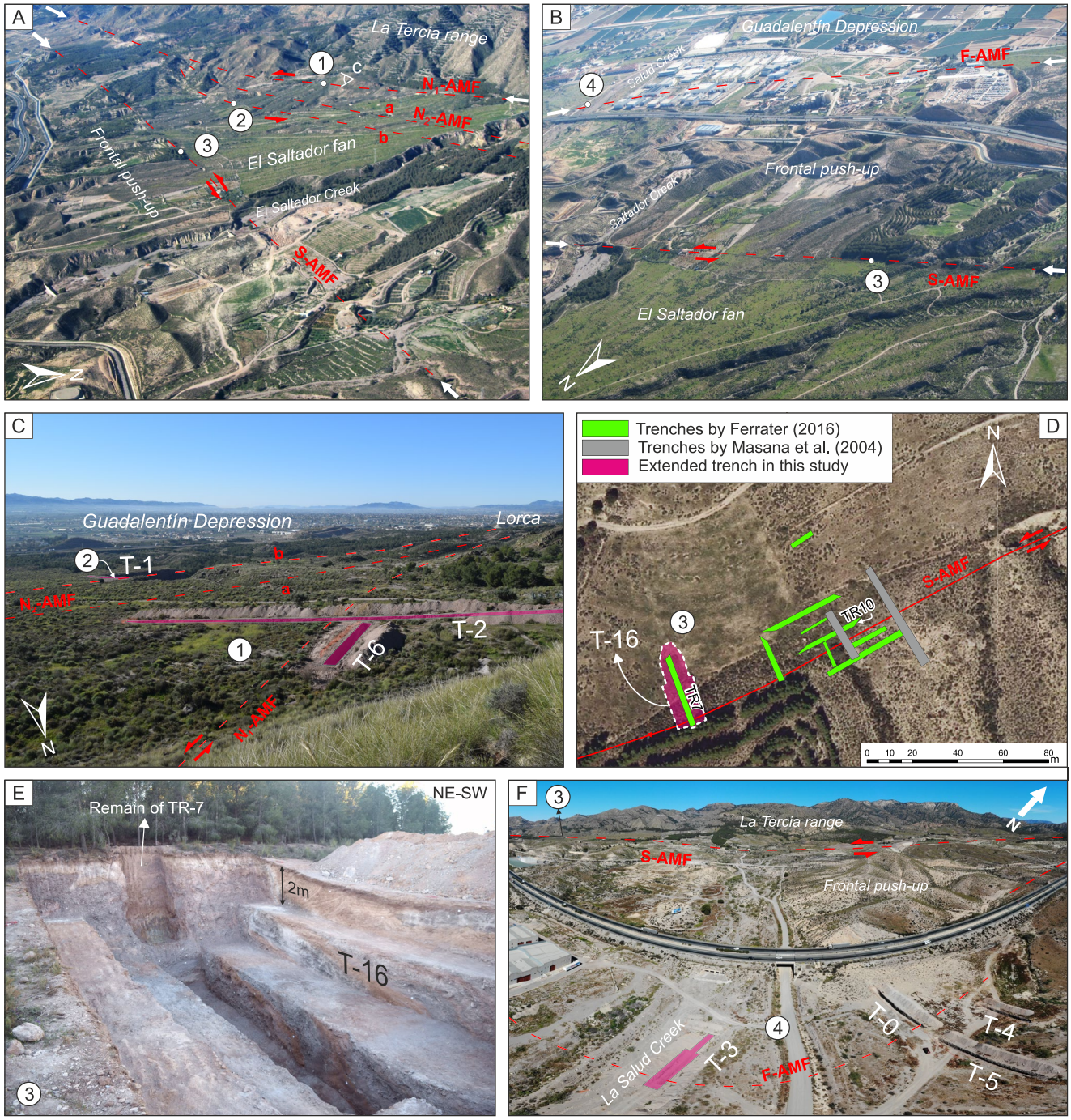

Figure 3. (a) Aerial view of El Saltador alluvial fan with the location of the paleoseismic sites in it (La 1: Tercia, 2: El Roser and 3: El Saltador). The geomorphological scarps and lineations generated by the most prominent fault branches (N_1-AMF and S-AMF) are indicated with a dashed red line. (b) Aerial view of the frontal pressure ridge with the traces of the limiting fault branches indicated, as well as the location of the respective paleoseismic sites (3: El Saltador and 4: La Hoya). (c) Detail view of La Tercia and El Roser sites, with the location of the trenches (magenta) respective to the fault branches. (d) Plan view of El Saltador site with the location of T-16 with respect to previous 3D trenches in that site (Ferrater, 2016 ; Masana et al., 2004). (e) Image of T-16 in El Saltador site, an exceptionally deep paleoseismic trench (~7 m) to capture the whole deformation generated by the S-AMF. (f) Aerial view of La Hoya site in the context of the frontal pressure ridge. The trenches used in this study are highlighted in magenta (T-3).

Table 1
Dating Results of the Sedimentary Units

Optically stimulated luminescence (OSL)

Fault	Sample ID	Depth (m)	Moisture (%)	Dose rate (Gy/ka)	Absorbed dose (Gy)	Method	Measured/accepted aliquots	Outliers (number/%)	Statistical model	Age ± 1σ (kyr BP)
N_{2b}-AMF	T1-OSL-1[a]	0.9	9 ± 4	3.65 ± 0.18	X ± X	MG	np	np	CAM	Out of range
	T1-OSL-4[a]	0.6	4 ± 4	3.01 ± 0.16	230.9 ± 11.7	MG	44/31	6	CAM	**76.8 ± 5.6**
	T1-OSL-6[a]	2.0	4 ± 4	3.08 ± 0.16	X ± X	MG	np	np	CAM	Out of range
	T1-OSL-7[a]	1.7	4 ± 4	3.48 ± 0.17	159.3 ± 8.2	MG	42/29	5	CAM	45.8 ± 3.3
	T1-OSL-9[a]	0.9	9 ± 4	3.78 ± 0.18	155.3 ± 4.4	MG	36/24	8	CAM	41.0 ± 2.3
S-AMF	SAL-27[b]	0.9	5 ± 2	3.36 ± 0.12	51.2 ± 4.7	MG	np	<5%	CAM	**15.2 ± 0.1**
	T16-OSL-3[c]	1.2	5 ± 3	2.45 ± 0.08	40.8 ± 1.6	MG	72/66	6	CAM	**16.7 ± 0.9**
	SAL-10[b]	1.7	5 ± 2	3.02 ± 0.14	61.0 ± 3.0	MG	np	np	CAM	**21.7 ± 1.6**
	SAL-24[b]	2.2	5 ± 2	3.30 ± 0.56	79.4 ± 3.7	MG	np	<5%	CAM	**31.2 ± 2.6**
	SAL-25[b]	1.9	5 ± 2	3.05 ± 0.49	127.1 ± 4.6	MG	np	<5%	CAM	**45.9 ± 3.5**
	SAL-26[b]	2.5	5 ± 2	3.24 ± 0.53	175.6 ± 7.2	MG	np	<5%	CAM	**73.4 ± 7.0**
	SAL-11[b]	1.1	5 ± 2	2.47 ± 0.11	>250	MG	np	np	CAM	>101[b]
F-AMF	T3-OSL-7[d]	5.2	11	2.4 ± 0.1	46 ± 4	MG	24/19	5	RM	19 ± 2
	T3-OSL-9[d]	1.0	15	3 ± 0.1	34 ± 4	MG	24/19	5	RM	11 ± 1
	T3-OSL-13[d]	4.6	7	2.02 ± 0.04	49 ± 5	MG	24/23	1	RM	**18 ± 1**
	T3-OSL-16[d]	1.4	12	2.6 ± 0.05	14 ± 4	MG	24/9	15	RM	5 ± 2

Radiocarbon

Fault	Sample ID	Sample type	Fraction of modern (pMC ± 1σ)	Radiocarbon age (years BP ± 2σ)	Calibrated age (years BP ± 2σ)
N_1-AMF	T2-cc-1[e]	Snail shell fragments (1–2 cm)	2.906 ± 0.042	28,424 ± 116	32,051–33,092
	T2-cc-2[e]		2.541 ± 0.039	29,502 ± 123	33,781–34,376
	T2-cc-3[e]		2.434 ± 0.038	29,848 ± 125	34,123–34,581
N_{2b}-AMF	T1-cc-1[e]		2.209 ± 0.040	30,627 ± 145	**34,630–35,336**
	T1-cc-2[e]		0.779 ± 0.028	39,000 ± 289	**42,384–42,907**
	T1-cc-6[e]		1.377 ± 0.033	34,424 ± 193	**39,205–39,996**
F-AMF	T3-ch-1[f]	Charcoal fragments (1–5 mm)	0.3724 ± 0.0012	7,935 ± 30	8,638–8,985
	T3-ch-2[f]		0.3453 ± 0.0037	8,540 ± 90	**9,306–9,759**
	T3-ch-3[f]		0.3803 ± 0.0013	7,765 ± 30	**8,449–8,600**

Note. The dates are obtained using OSL and radiocarbon techniques. The target mineral for luminescence is quartz. Outliers are the values excluded to calculate the absorbed dose distributions. Calibration of radiocarbon ages is done with the IntCal20 curve (Reimer et al., 2020) and OxCal v.4.3.2 (Ramsey, 2017). The position of the samples is found in Figures 7 and 8. The dates highlighted in bold are the ones used for the slip rate analysis of this study. CAM: Central Age Model (Galbraith & Roberts, 2012); RM: Robust Mean (using Robust Statistics V1.0; AMC, 2001); np: not provided by the laboratory; MG: multi-grain aliquots (quartz). pMC: percent modern carbon.

[a]Samples dated at CENIEH (Burgos, Spain). [b]Dates carried out by Ferrater (2016) at the El Saltador site (see Supporting Information S1 for technical details on these dates). [c]Sample dated at the University of Cologne (Germany). [d]Samples dated at the Instituto Tecnico Superior (Lisboa, Portugal). [e]Samples dated at the DirectAMS Laboratory (Bothell, USA). [f]Samples dated at the KCCAMS facility, University of California (Irvine, USA).

4. Structure and Kinematics of the Fault Branches Across the Transect

From the geomorphological and structural mapping, we recognize at least five subparallel fault branches showing clear surface expression and late Quaternary deformation in a ~2 km-wide NE–SW-striking fault zone. Except for the northwesternmost branch, the other four strands are well-expressed in the fault-parallel sector between Lorca and the La Salud Creek (Figure 2), while to the SW and to the NE, the fault zone loses surface expression, becoming more evident in the morphology a single fault trace (Figure 1c). The apparent loss of fault expression might reflect a decrease in its activity, but it might also be due to the lack of geomorphological markers such

as alluvial surfaces or displaced/deflected drainages, and the predominance of erosive processes exposing the Miocene basement rocks.

Previous studies identified three of the five fault strands for the northern (N-AMF) and central sectors (S-AMF) (e.g., Martínez-Díaz, 1998; Martínez-Díaz & Hernández-Enrile, 2001), and the frontal zone (Ferrater et al., 2017). In this study, we provide a more detailed mapping of two additional fault strands and show evidence of the Quaternary paleoseismic activity for all five of them. Based on that, we name each fault branch as follows (Figure 2): N_1-AMF, N_{2a}-, and N_{2b}-AMF referring to the three branches of the northern sector (N-AMF), S-AMF refers to the central sector, and F-AMF refers to the frontal part of the system. Both S-AMF and F-AMF, and N_{2a}- and N_{2b}-AMF bound the limits of two push-up structures (Figure 2b).

The fault branches affect different generations of Quaternary alluvial fans that drain from the ranges that are uplifted by the AMF in the NW (La Tercia range) toward the Guadalentín Depression to the SE. Four generations of alluvial fans are defined from the Middle Pleistocene to the Holocene, as described by Silva (1994) and Martínez-Díaz et al. (2003). The older generations (Q4 and Q3) are mostly spatially limited between the main mountain front (N_1-AMF) and the central branch (S-AMF). One of the main examples of this generation is the El Saltador alluvial fan, along which the La Tercia, El Roser and El Saltador sites are located (Figures 2 and 4). The Q2a surface, which represents a transitional generation to Q2, is coeval with the late Q3 generation at some points (see Section 5.2) and is usually restricted to proximal areas of the mountain front (Figure 2a). The Q2 alluvial fans are incised into the Q3 and Q4 deposits and extend farther from the mountain fronts toward F-AMF. The Q2 generation is not active albeit not completely disconnected from the drainage channels. Q1 represents the active alluvial and fluvial systems, located in the center of the Guadalentín Depression. The scarce relief of this lowland area and the extensive agriculture makes it difficult to recognize all alluvial landforms. We therefore map them as a uniform polygon that includes deposits from alluvial fans and floodplains river areas.

4.1. Fault Branches and Slip Partitioning

The five fault branches of the Lorca-Totana segment define three structures that can be distinguished at the surface (Figure 2b): a major mountain front (N_1-AMF) and two push-up structures; one central (N_{2a}- and N_{2b}-AMF) and one in the front (S-AMF and F-AMF). The slip is partitioned among these five branches; three show predominant vertical throw while the other two accommodate strike slip, as we detail below. We describe each fault from NW to SE, and their deformation is depicted in Figures 5–8.

4.1.1. Mountain Front (N_1-AMF)

The N_1-AMF fault strand represents the northernmost identified limit of the fault zone, bounding the La Tercia range mountain front with an average N55° strike, changing to N35°–N41° at the El Saltador fan (Figure 2a). In outcrops, the fault is displayed with a subvertical or strong dip to the NW (70°–90°) affecting materials from the metamorphic basement of the La Tercia range and Quaternary alluvial materials. In older materials, the fault zone presents shear bands with incohesive fault breccias and clay-rich gouges developed up to widths over tens of meters (e.g., Figure 5b), which evidence the long-term activity of this fault strand. In the Late Pleistocene alluvial fan deposits (30–40 ka; see dates in Table 1), the fault generates discrete subvertical fractures with clast lineations, and lack the deformation recognized in the underlying basement rocks, (Figure 5a). This evidence is expected due to the much younger age of the deposits and therefore less cumulative deformation.

Although the N_1-AMF is the geomorphological limit of the La Tercia range (Figure 3f), which indicates a major vertical component in the past, the kinematic evidence in Late Pleistocene materials suggests a predominantly strike slip motion, as evidenced by the following observations:

1. Fault plane striae in two basement outcrops along the fault branch show rakes of 2°–20° (Figure 5b).
2. Absence of significant vertical separations or scarps in the Quaternary alluvial fans (mainly Q2) at the La Tercia site (see log of T-2 in Figure 7).
3. Stratigraphic incoherence of apparent fault offsets; for example, smaller vertical separations in older materials than in younger (Figure 5a).
4. Presence of left-laterally deflected channels, such as San Julián and El Saltador creeks (Figure 4).

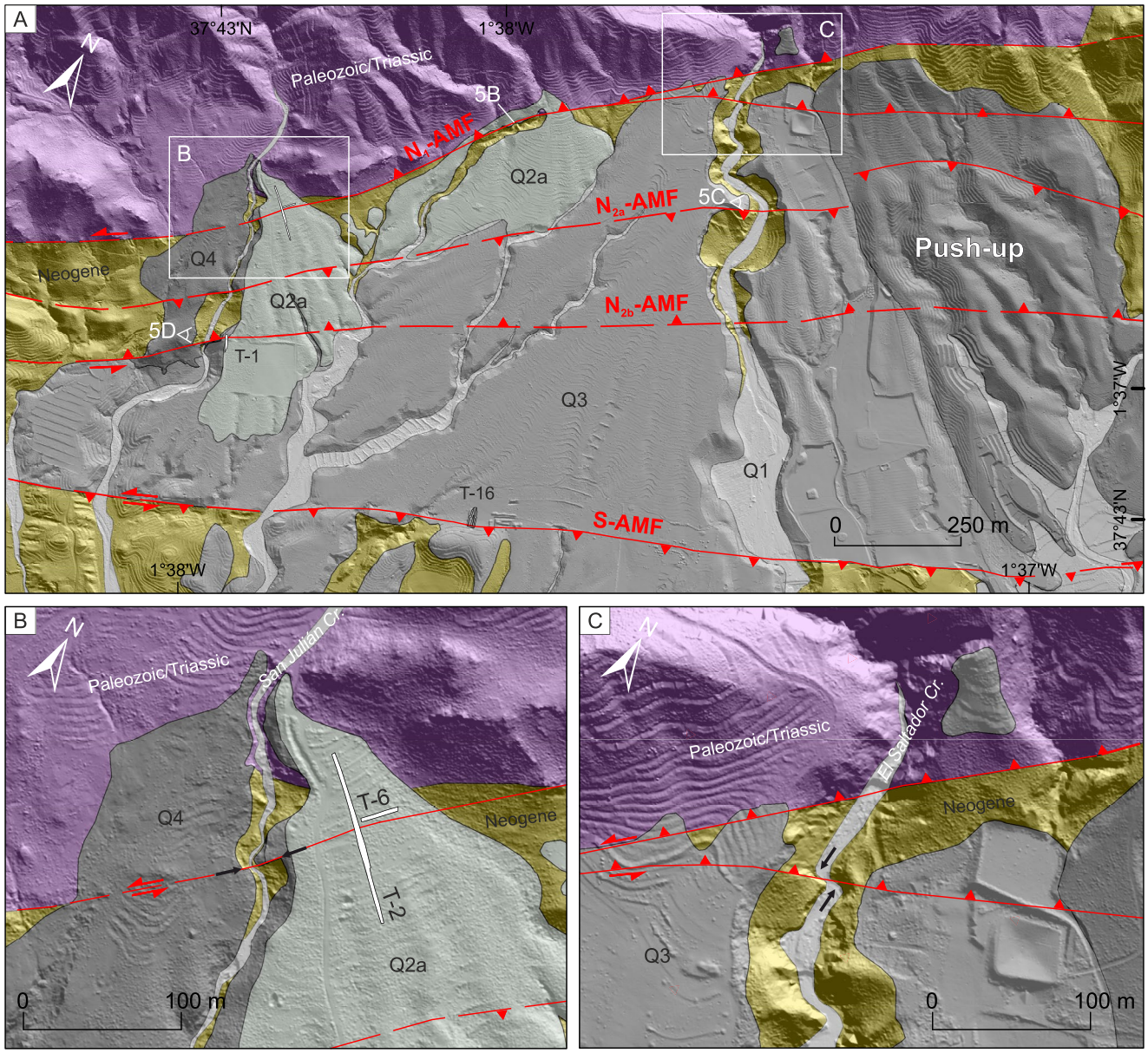

Figure 4. (a) Geological mapping of the northern sector of the Lorca-Totana segment. See Figure 2 for the legend of the geological units depicted. Note that the map location of the outcrops shown in Figures 5c and 5d are indicated in this figure. (b) Detail of the geological map surrounding the La Tercia site. Note that the left-lateral dislocation of the San Julián Creek margin is indicative of the strike slip kinematics of the N_1-AMF. (c) Detail of the left-lateral dislocation in the El Saltador Creek related to the activity of the N_1-AMF.

4.1.2. Central Push-Up (N_2-AMF)

The N_2-AMF push-up structure is part of the northern sector of the AMF and is formed by two subparallel branches that define a push-up. This push-up is bounded by a synthetic fault (N_{2b}-AMF) to the south and by an antithetic fault (N_{2a}-AMF) to the north, both with a mean strike of N55°–N58° and with opposing 70°–80° dips. Along its trace, the N_{2a}-AMF merges into N_{2b}-AMF coinciding with strike bends of the former, such as SW of the La Carraclaca or near the San Julián Creek (Figure 2a). The merging of the surface faults suggests that both strands join at depth along most of their length.

The surface footprint of this structure is marked by ∼1–2 m high fault scarps in the Quaternary alluvial fans. The deformation pattern for both branches is controlled by near vertical monoclinal propagation folds (Figures 5c and 5d) affecting the Tortonian marls substratum up to the Quaternary alluvial deposits (Q2 and Q3). Along the

Figure 5. (a) N_1-AMF fault strand in young Q2 materials in the walls of T-2. Incongruent separations can be seen along the fault, evidencing lateral displacement. (b) NW-dipping fault zone of the N_1-AMF in basement materials, with deformation bands: incohesive fault breccias and clay-rich gouges. Notice that in this area the fault puts in contact Paleozoic and Miocene materials. (c) Outcrop of the N_{2a}-AMF in the northeastern margin of the El Saltador Creek, where the fault affects the whole Quaternary sequence and generates a geomorphological bump on the surface. (d) Outcrop of the N_{2b}-Alhama de Murcia Fault (AMF) in the NE margin of the San Julián Creek where the fault generates a verticalized monoclinal fold in the Q4 (Cg unit) materials.

N_{2a}-AMF, the fold geometry is observed at the El Saltador Creek, with a ~10 m vertical separation of the unconformity between the Q3 and the Tortonian basement propagating upwards (Figure 5c). In the N_{2b}-AMF, the fold geometry is controlled by a highly cemented alluvial unit (Cg unit henceforth) that describes a monoclinal fold with a ~20 m vertical separation in the San Julián creek margin (Figure 5d). This unit is the base of the Quaternary deposition in the study area and overlies the pre-Quaternary paleoreliefs (mostly Tortonian calcarenites

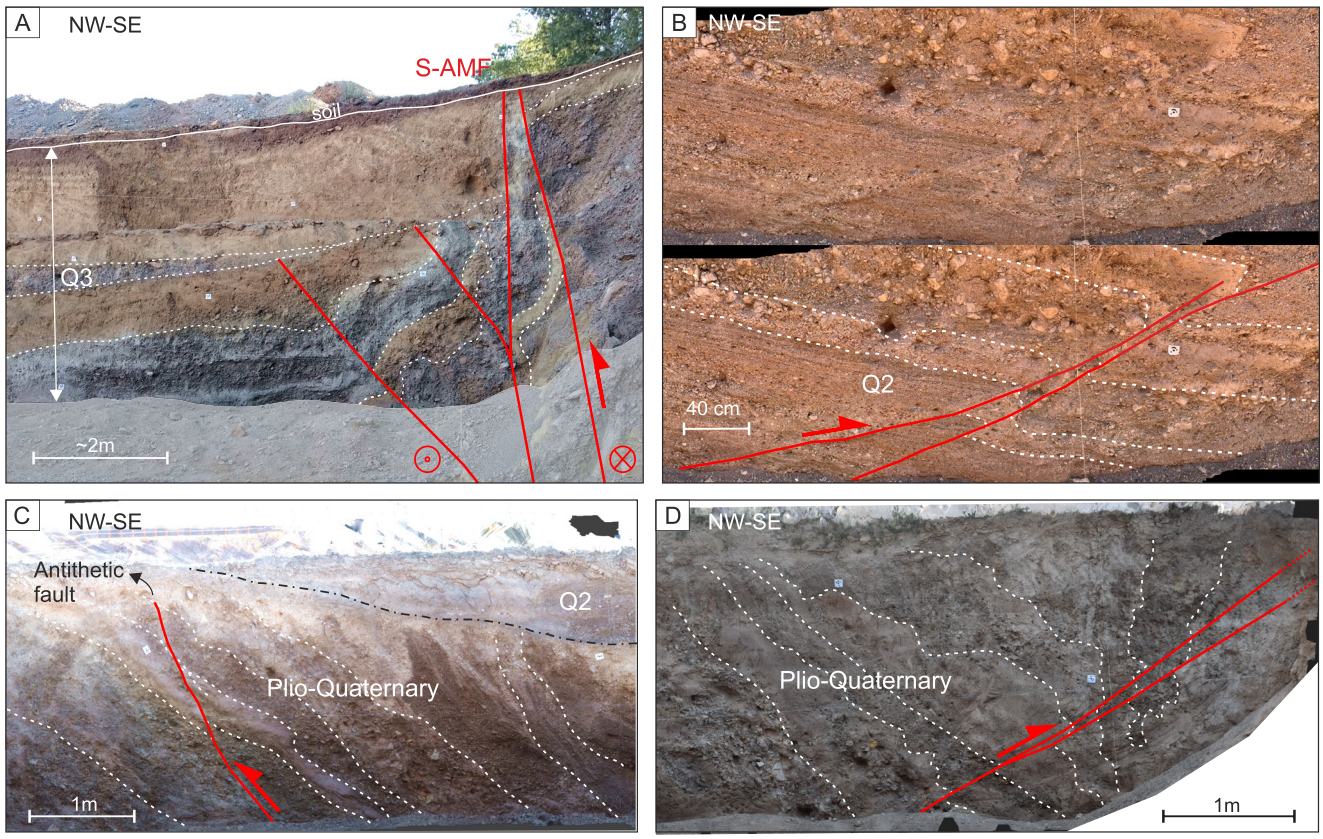

Figure 6. (a) Detail image of the S-AMF fault zone in El Saltador site (T-16) affecting Q3 alluvial materials. The structure shows a positive flower geometry typically found in strike slip systems. (b) Detail of the F-AMF and associated displacements in Q2 alluvials within T-3. (c) Deformation associated with antithetic faults of the F-AMF in Plio-Quaternary alluvial materials of T-4; intense shear deformation and monoclinal tilting. (d) Picture of F-AMF in Plio-Quaternary alluvial materials generating intense tilting and shear of the units in T-1.

and marls) with an irregular topography. In both branches, the deformation decreases to the surface with angular unconformities, which support their repeated tectonic activity (Figures 5c, 5d, and 7).

The N_2-AMF push-up has a strong vertical throw component evidenced by the (Figures 5c and 5d):

1. Presence of significant vertical separations related to fault-propagation folding (e.g., Cg unit).
2. Presence of fault scarps at the alluvial fan surfaces associated with the trace of the push-up structure.

The strike slip component is likely present here as well, especially considering the steep dips of the faults (Figures 5c and 5d) and the fact that push-up structures are typically formed in strike slip fault zones. However, the geomorphic evidence of lateral component along this push-up is unclear in the study area. For instance, the right lateral channel deflections observable at the top of the El Saltador fan (Figure 4a) can be explained by the re-adjustment of the drainage to the uplift generated by the push-up. 3D trenching is therefore required to properly characterize the strike slip component.

4.1.3. Frontal Pressure Ridge (S-AMF and F-AMF)

The frontal pressure ridge has an average ~N65° strike and is limited by two principal fault branches (S-AMF and F-AMF).

4.1.3.1. S-AMF

The northern bounding fault, S-AMF, is the most geomorphologically and structurally prominent branch of the AMF, with a fault zone that can reach up to dozens of meters in thickness (Martínez-Díaz, 1998). Such a prominent expression explains why all previous paleoseismic studies along the Lorca-Totana segment have been conducted on this branch.

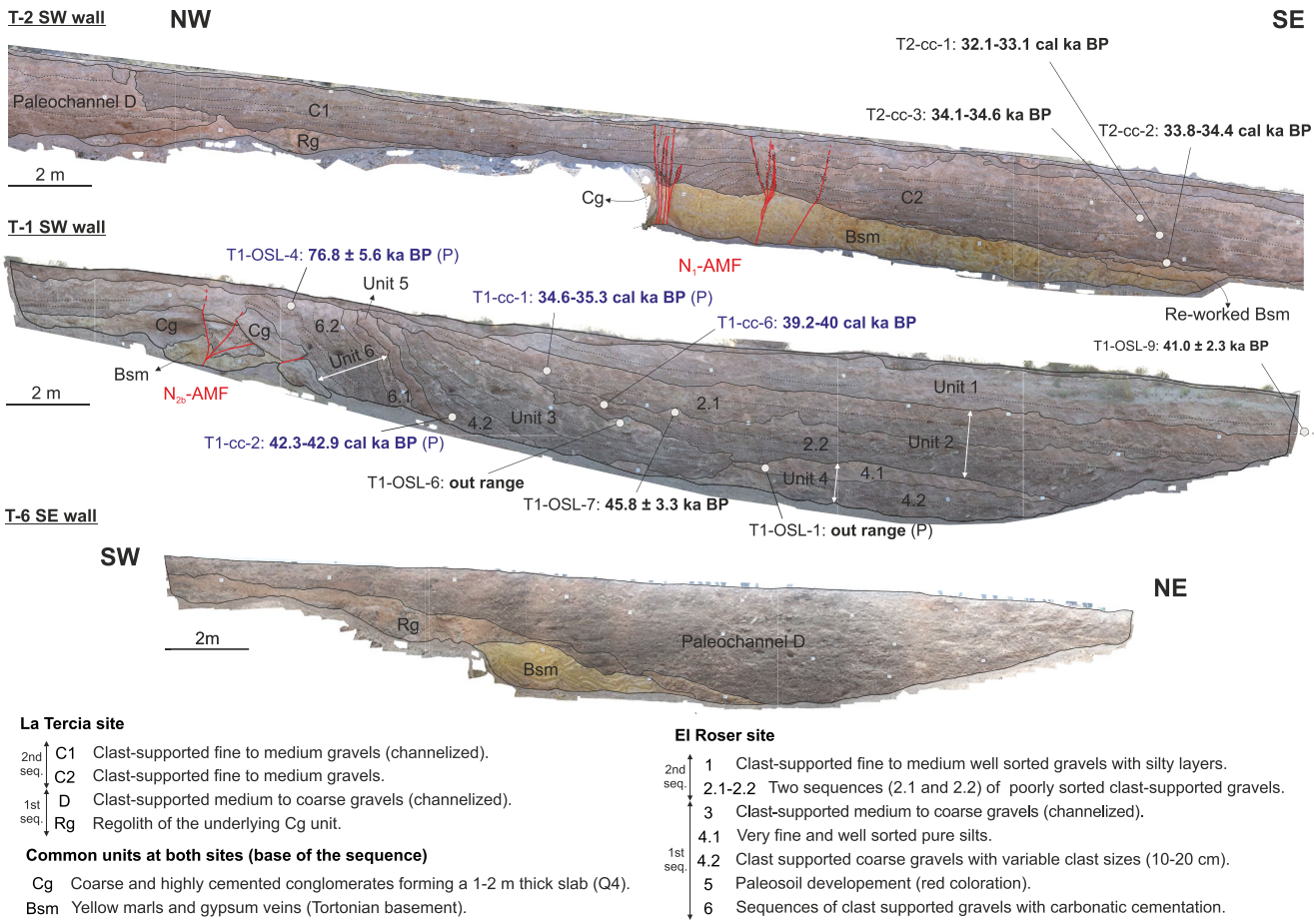

Figure 7. Interpreted trench photologs of T-2 and T-6 at the La Tercia site, and T-1 at the El Roser site. The samples and resulting numerical dates of the stratigraphy are indicated. The dates located in the opposite trench wall than the depicted in the figure are projected into the same stratigraphic position and indicated with the descriptor "(P)." The blue dates are the ones selected for the slip rate analysis. Note that all trench walls have been mirrored to follow a consistent down-slope (left to right) orientation. To observe full uninterpreted logs of both walls, as well as the complete length of T-2, see Gómez-Novell et al. (2022).

Structurally, the S-AMF dips subvertically, uplifting the SE block, and generating a SW–NE scarp and elongated relief that, along with F-AMF, form the pressure ridge. The fault zone is defined by upturned Quaternary alluvial deposits in the footwall (Figure 6a), in contact with the Tortonian basement ridge in the hanging-wall (Figure 2a). In addition, secondary synthetic SE-dipping faults form a positive flower structure with NW-verging propagation folds in the Quaternary sequence (e.g., El Saltador site; Figures 6a and 8). These accommodate an important part of the vertical component of this fault, and generate a counter-slope scarp that acts as a sedimentary trap for the alluvial flows, making it a unique site for the preservation of the fault's morphogenetic history (Ferrater et al., 2016).

Kinematically, the S-AMF is predominantly strike slip as characterized in previous studies at the El Saltador site (inferred 8–10 times the vertical from Ferrater et al., 2016). The main evidence is the presence of laterally offset active streams (Ferrater et al., 2015; Martínez-Díaz, Masana, & Ortuño, 2012) and laterally offset paleochannels crossing the fault, as demonstrated by 3D trenching (Ferrater et al., 2016). Despite this, we observe that the S-AMF has a significant vertical component associated with the propagation folds in the footwall (Figure 6a).

4.1.3.2. F-AMF

The F-AMF constitutes the SE limit of the pressure ridge, the southernmost branch of the AMF known to date, and likely the frontal structure of the entire AMF bounding the Guadalentín basin. The F-AMF has an irregular trace with relay zones, such as NW of the La Hoya site (Figure 2a), and its surface location is mainly inferred by the geomorphological limit of the pressure ridge. Direct observations of this fault are mainly from the

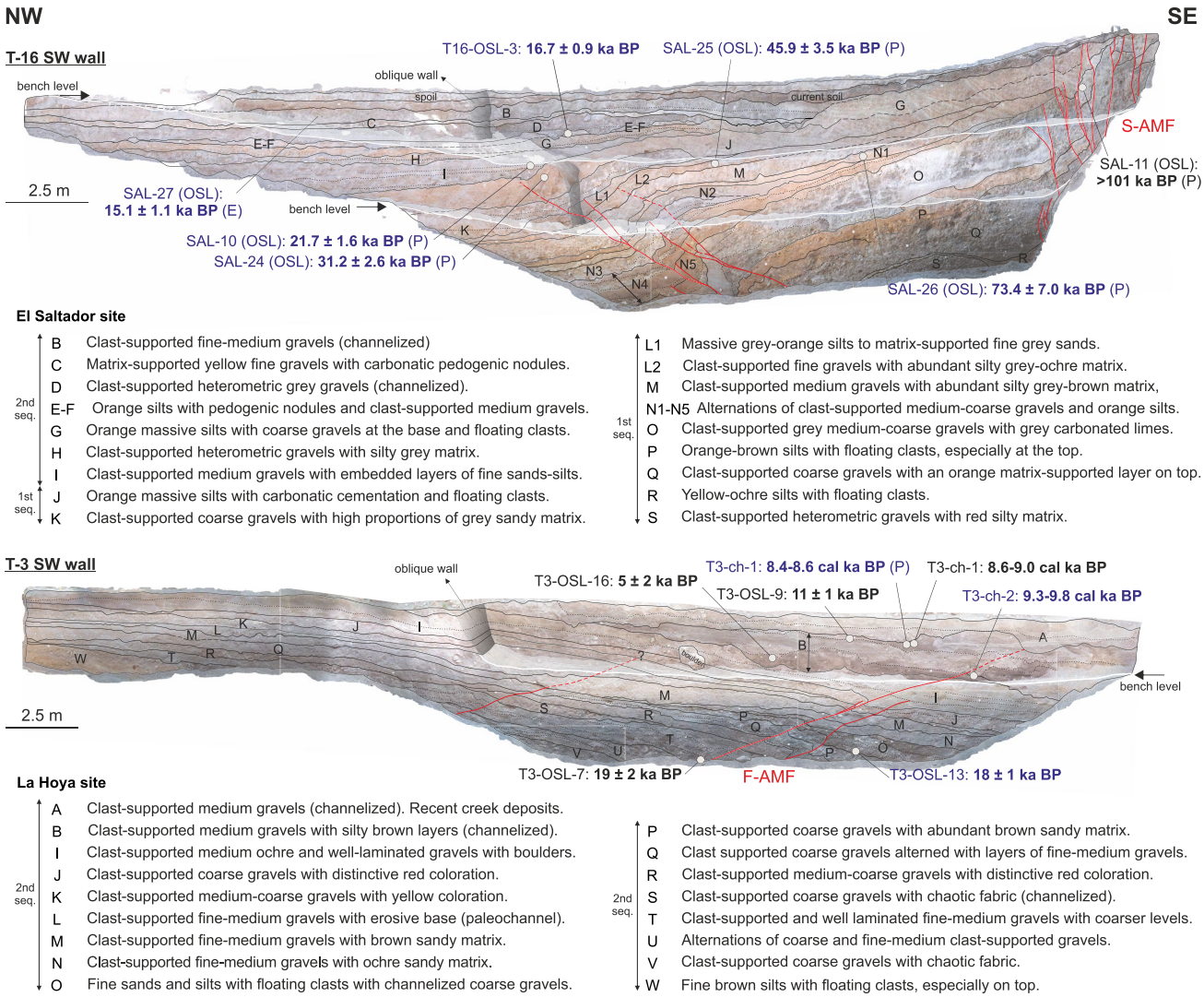

Figure 8. Interpreted trench photologs of T-16 and T-3 in El Saltador and La Hoya sites, respectively. The samples and resulting numerical dates of the stratigraphy are indicated. The dates located in the opposite trench wall than the depicted in the figure are projected into the same stratigraphic position and indicated with the descriptor "(P)." Similarly, in T-16 the date of unit B, which is extrapolated from a previous trench in El Saltador site (TR-10; Ferrater, 2016; Ferrater et al., 2016), is indicated with the descriptor "(E)." See Figure 3d for the location of TR-10. The blue dates are the ones selected for the slip rate analysis. Note that both trench walls have been mirrored to follow a consistent down-slope (left to right) orientation. To observe full uninterpreted logs of both walls, see Gómez-Novell et al. (2022).

paleoseismic survey at the La Hoya site and the road cut described by Ferrater (2016, p. 53). Its diffuse expression can be explained by the younger age of materials affected (Q2), which implies less cumulative tectonic activity. Moreover, the intense anthropic activity in this sector further obscures the surface expression of the fault.

The F-AMF is a low angle NW-dipping (~20°) reverse fault (Figure 6b). In Plio-Quaternary deposits, the fault is associated with strong tilting, folding, localized shear zones and SE-dipping faults interpreted to be antithetical to the principal NW-dipping structure (Figures 6c and 6d). In Q2 deposits the deformation is more subtle, with small decametric scale on-fault slips and with the most part of the deformation accommodated by a low angle monoclinal propagation fold (see T-3 log in Figure 8). The differential deformation between deposits suggests repeated activity in this branch throughout the late Quaternary.

Kinematically, we identify this fault as mainly dip-slip. The supporting evidence are:

1. Dipping angle of ~20°, unusually low for a strike slip fault.
2. Absence of laterally offset or deflected features along the fault trace.

3. Lack of strike slip evidence in the affected sediments. For instance, fault offsets are stratigraphically concordant (decreasing to the surface) (Figures 6b and 8).

5. Paleoseismic Trench Results

Paleoseismic trenching was carried out along four of the five active branches of the Lorca-Totana zone across a NW–SE transect (Figures 2 and 3). The La Tercia site is along the N_1-AMF, the El Roser site is along the N_{2b}-AMF, the El Saltador is along the S-AMF and the La Hoya is along the F-AMF. Paleoseismic results are extracted from all trenches, except from T-0, T-4, and T-5 at the La Hoya site where recent Quaternary deformation is not recorded. Notably, the N_{2a}-AMF has not been studied because we could not identify a good trenching location.

5.1. Stratigraphy

The sediments exposed in the trenches belong mainly to the Q3 and Q2 alluvial fan generations. However, at the El Saltador fan, the base of the Quaternary deposits is formed by the Cg unit (part of Q4), made of a 1–2 m thick, highly cemented conglomerate. This unit lies on top of Tortonian yellow marls and calcarenites and crops out mainly in the proximal parts of the fan (La Tercia and El Roser sites) where the Q2 and Q3 deposits are thinner (Figure 7).

The stratigraphy over the Cg unit is divided into two sequences of deposits corresponding to the Q3 and Q2 generations. The lower (older) sequence is formed by clast supported coarse to medium heterometric and subangular conglomerate interpreted to be debris flow and sheet flow deposits (Q3). This sequence is related to the proximal alluvial activity and is represented by different units: unit Rg to D in T-2, unit D in T-6, units 6 to 3 in T-1 and units S to J in T-16 (Figures 7 and 8). The second (younger) sequence represents a change in the depositional environment to a channelized alluvial regime formed by clast-supported gravels with planar and localized crossed bedding. The sequence is formed by the late Q3 generation and transitional Q2a generation, and culminates with the Q2 generation in the frontal part (Figure 2a). This sequence is incised into the older deposits, marking the onset of the abandonment of the alluvial fans and migration of the drainage toward the Guadalentín Depression (Martínez-Díaz et al., 2003; Silva et al., 1992); see Section 5.2 and dates in Table 1. In the trenches, the sequence is formed by units C2 and C1 in T-2, units 2 and 1 in T-1, and unit I up to the current soil in T-16. At the La Hoya site (see location in Figure 2a), all of the exposed stratigraphy in T-3 corresponds to this younger sequence (Q2), culminating with deposits from the active La Salud Creek (units B and A; Figure 8). This sequence is deposited unconformably on top of strongly cemented Plio-Quaternary alluvium that crops out in T-4 (Figure 6c).

The nomenclature used for the units is different for each site, hence similar names do not imply correlation, except for the Cg unit that is common for both the La Tercia and El Roser sites. In T-16 at the El Saltador site we adopt the unit nomenclature used by Ferrater et al. (2016) and we define sub-units to those strata where we observe better stratigraphic resolution (e.g., units N1, N2, N3 for unit N; Figure 8).

5.2. Age Control

The age control of the units is crucial to estimate the rates of the deformation on each fault branch. Table 1 compiles the dating results of the samples from each trench. Out of the 19 new samples, 8 are ultimately selected for the slip rate estimates because they are either the ones that yield better stratigraphic coherency or show smaller uncertainties than other dates from the same strata. For instance, in T-1, the radiocarbon dates of units 2.1 and 2.2 provide smaller uncertainties, hence we select them over the OSL ages (Table 1). Similarly, in unit B of T-3 we select the three radiocarbon dates over the OSL because the latter are incoherent with the stratigraphy (T3-OSL-16 is younger than T3-OSL-9; Figure 8). In addition, the age of T3-OSL-16 is based on the measurement of only 9/24 aliquots (Table 1), which likely yields a less reliable age estimate. At the El Saltador site we use five of the six previous OSL dates from Ferrater (2016). Four of those dates are from TR-7 (location in Figure 3d), whose location makes the correlation to the trench walls of T-16 simple. The other date is extrapolated from a more distant trench (TR-10) at the El Saltador site, which dates unit B in T-16 (Table 1). For more details on samples and datings used from this study see the Supporting Information S1 of this paper.

The base age of the Quaternary deposits (Cg unit) of the area is not determined in our study. However, Martínez-Díaz and Hernández-Enrile (2001) dated this unit near the La Carraclaca site using the U/Th technique on the travertines developed on top of the unit. Although the results were highly variable depending on the stratigraphic position sampled, its minimum age was estimated to be 198 ± 6.5 ka (Upper Middle Pleistocene), which we adopt here. Above the Cg stratum, the older Late Pleistocene alluvial sequence at the El Saltador fan ranges from >101 (SAL11) to 42.6 ± 0.1 ka (T1-cc-2) in the proximal parts of the fan (T-1), or to 31.2 ± 2.6 ka (SAL24) in the distal parts (T-16) (Figure 2a). During this time period, the alluvial sedimentation was active between the N_1-AMF and S-AMF, as revealed by the deposition of the El Saltador fan. The onset of the younger sequence started in the proximal parts at 39.6 ± 0.2 ka (T1-cc-6) and extended until at least to 35–32 ka (T-2 samples in unit C2). In the central parts (e.g., El Saltador site), the sequence started later around 21.7 ± 1.6 ka (SAL10) extending up to 15.2 ± 1.1 ka (SAL27). Because the Q2a is not present in this sector (Figure 2a), the onset of the younger sequence necessarily belongs to the upper part of the Q3 generation. These data suggests that both generations coexisted in time at different sectors of the fault and indicates that the younger deposition was migrating toward the south. From this point we interpret the fan deposition between N_1-AMF and S-AMF to be practically abandoned, with only a few small channels developed in recent years (unit A; Ferrater et al., 2016). The age of abandonment and migration of the alluvial systems to the frontal parts of the range is consistent with the age of the lower units in T-3 at the La Hoya site (18 ± 1 ka; T3-OSL-13). There, the alluvial deposition lasted at least until 8.53 ± 0.04 ka (T3-ch-3), and afterward, the incision of the current creeks (e.g., La Salud) progressed to the Guadalentín Depression, feeding the Q1 fans.

The alluvial deposition in the area is typically intermittent and therefore can lead to gaps (hiatuses in deposition) throughout the stratigraphic sequences. The largest gaps appear in the apical parts of the El Saltador fan, where erosion dominates, as opposed to the tectonic barrier at the El Saltador site. At the El Roser site, for instance, gaps are identified between units Cg and 6 (∼120 kyr), and between units 6 and 4.2 (∼35 kyr) (Figure 7). Moreover, the lack of recent sedimentary record since ∼35–32 ka is also remarkable in this sector (La Tercia and El Roser).

Lastly, some of the samples (T1-OSL-1 and T1-OSL-6; Table 1) could not be dated due to the absorbed dose of the sample being out of the detection range of the method. Given that these samples are in higher (younger) stratigraphic positions than others that are successfully dated (e.g., T1-OSL-4), and thus cannot be older than the detection age range for the OSL, we estimate that they might be affected by inheritance of luminescence signal or quartz minerals with different characteristics. We suggest that the most likely justification are that quartz grains were not properly bleached during a short transport and deposition, consistent with the short distance of the El Roser site to the source area of the alluvials sampled (La Tercia range).

5.3. Fault Deformation

Fault vertical throw and strike slip are measured for each fault branch according to their predominant kinematics. Vertical throw across the N_{2b}-AMF (T-1), S-AMF (T-16) and F-AMF (T-3); strike slip across the N_1-AMF and S-AMF.

5.3.1. Vertical Throw

We measure the vertical throw of the different stratigraphic horizons that delimitate unit blocks with clear differential deformation at the N_{2b}-AMF, S-AMF and F-AMF strands (e.g., angular unconformities, decreasing fault offsets) (Figure 9). At the N_1-AMF we calculate the throws indirectly from the fault strike, and then the net slip considering a 2°–20° rake range based on field measurements (Equations S1 and S2 of the extended methods in Supporting Information S1). A 2° rake is the most consistent with the local <1 m vertical separations in T-2 (Figures 5a and 7), although this might be a local effect and an apparent separation related to the strike slip. Conversely, a 20° rake yields vertical throws of 8.6–10 m, which help to explain the important uplift associated with the Quaternary materials in the mountain front of the La Tercia range.

Table 2 summarizes the vertical throws measured in each trench. It should be noted that, in general, all the vertical throws here could be apparent to some extent because of (a) the lateral component of the fault branches (especially N_1-AMF and S-AMF), and (b) the fact that the trenches might not be excavated completely parallel to the shortening direction.

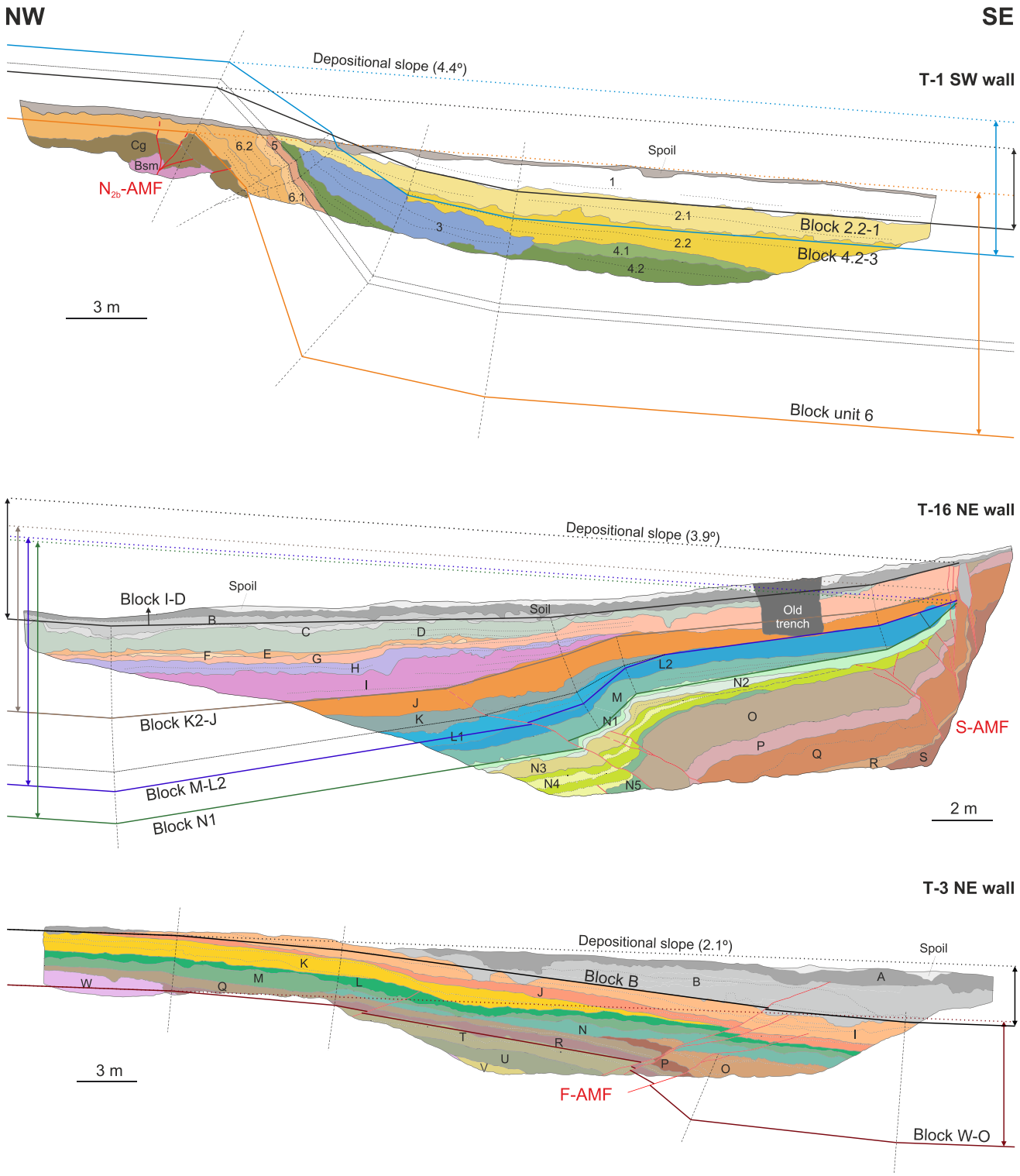

Figure 9. Structure simplification of T-1, T-16 and T-3 to calculate vertical throws (see details in Text S1 and Figure S1 in Supporting Information S1). Note that the measured throws are a minimum in units that do not entirely crop out in the trench because the dips and fault-displacements are adopted from younger and less deformed units. Also, in T-16, the lack of observation of the units in the SE block of the fault further emphasizes this minimum. The schemes presented here correspond to a single wall per trench and a single position of the unit contact. The trench wall from T-1 has been mirrored to follow a consistent down-slope (left to right) orientation.

Table 2
Vertical Throw, Strike and Net Slips of the Trenches

Unit block	Age (ka)	Vertical throw ± 1σ (m)		Strike slip ± 1σ (m)	Net slip ± 1σ (m)
N_1-AMF					
Unit D	Minimum of 42.6 ± 0.2	2° rake	20° rake	$25.3^{+2.6}/_{-1.5}$	$25.3^{+2.6}/_{-1.5}$
	Maximum of 76.8 ± 5.6	0.8–1 ± 0.03	8.6–10 ± 0.4		
T-1 (N_{2b}-AMF)					
Unit 6	76.8 ± 5.6	7.6 ± 0.7		–	7.9 ± 0.7
Units 4.2 to 3	42.6 ± 0.2 (4.2)	4.3 ± 0.3		–	4.5 ± 0.3
Units 2.2 to 1	39.6 ± 0.3 (2.2) 35 ± 0.2 (2.1)	2.6 ± 0.2		–	2.7 ± 0.2
T-16 (S-AMF)					
Unit N1	Min. 73.4 ± 7.0 (N1)	10.1 ± 0.3		39.4 ± 1.2	40.7 ± 1.2
Units M to L2	Min. 45.9 ± 3.5 (L2)	8.9 ± 0.2		34.8 ± 0.8	35.9 ± 0.8
Units K2 to J	Min. 31.2 ± 2.6 (J)	6.8 ± 0.3		26.5 ± 1.2	27.4 ± 1.2
Units I to D	21.7 ± 1.6 (I)	4.3 ± 0.2		$16.3^{+2.7}/_{-0.3}$	$16.8^{+2.7}/_{-0.3}$
	16.7 ± 0.9 (E)				
	15.2 ± 1.1 (B)				
T-3 (F-AMF)					
Units W to O	Min. 18 ± 1 (O)	5.2 ± 0.2		–	15.2 ± 0.6
Unit B	8.5 ± 0.04 (B top)	2.2 ± 0.2		–	6.4 ± 0.6

Note. The measurements are provided for the different deformed blocks dated in N_1-AMF, N_{2b}-AMF (T-1), S-AMF (T-16), and F-AMF (T-3). Out of the I-D block, the strike slips from T-16 are indirectly inferred (analytically derived) from the rake and vertical throw. See text for details. All values correspond to the median and 1σ intervals. Blank fields mean "undetermined."

5.3.2. Strike Slip

The strike slip in N_1-AMF is provided by the offset of the paleochannel observed in T-2 and T-6 (paleochannel D) with respect to the modern creek to the NE, interpreted as its source (Figure 10). The estimated lateral offset is $25.3^{+2.6}/_{-1.5}$ m (mean and 1σ interval) (Table 2). This value is a maximum because we cannot ignore that the paleochannel might be buried under the fan surface on the SE block of the fault. Moreover, the deepest exposure of paleochannel D in T-6 is assumed as the thalweg position (Figure 10c), which also yields a maximum displacement value. In this line, 3D trenching is encouraged to refine the position of this paleochannel. In S-AMF we adopt the lateral offset of unit D ($16.3^{+2.3}/_{-0.3}$ m) from Ferrater et al. (2016). According to those authors, the offset measured for this unit (not to be confused with paleochannel D in N_1-AMF) is the most reliable out of the various features measured. In the N_2-AMF push-up, despite acknowledging that the strike slip component is likely present due to the nature of the structure and its high-angle dip (70°–80°), we are not able to identify clear offsets and datable markers. Hence, for this fault strand the net displacement is a minimum solely based on the vertical throw.

5.3.3. Measurement of Net Slip

Fault net slips are inferred from the vertical and strike slip components and fault dip. The dips considered are: 80° for the N_1-AMF, 75° for N_{2b}-AMF, 90° for the S-AMF and 20° for F-AMF. For the N_{2b}-AMF and F-AMF, only dip slips are calculated due to the absence of strike slip characterization. In N_1-AMF we compute net slips of $25.3^{+2.6}/_{-1.5}$ and $26.9^{+2.7}/_{-1.6}$ m, based on the 2–20° rake range, respectively. In S-AMF, the arctangent of the quotient between the vertical throw and strike slip of unit D (Table 2) yields a fault rake of ∼14.8° (see Equation S3 of the extended methods in Supporting Information S1). We then use this rake to compute the strike and net slips of the other T-16 units from the observed vertical separations.

6. Geological Slip Rates

We compute the slip rates for each fault branch (Table 3) and sum the slip rates for all four branches that we analyze to resolve the overall slip rate of the fault system.

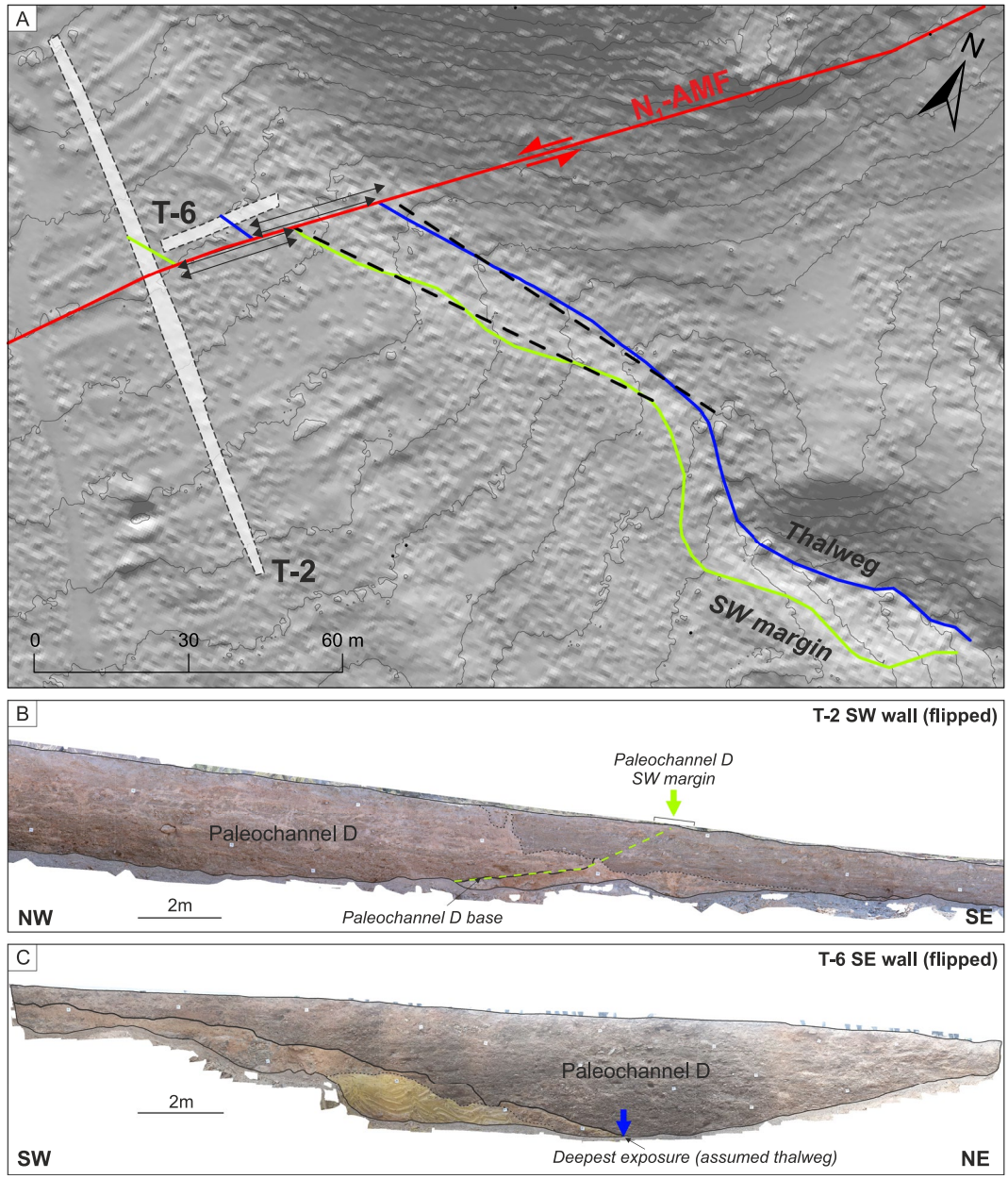

Figure 10. Estimation of the lateral slip of the N_1-AMF, based on Gold et al. (2011) method. (a) Plan view of the displaced features (right margin and thalweg) of paleochannel D and an active channel in each side of the fault. Downstream of the fault, the intersection of the channel features with the fault are used as piercing points. To capture better the average orientation of the channel, a linear regression is also approximated to the features and projected into the fault, resulting in another pair of piercing points. Upstream these features are projected using the paleochannel orientation observed in T-2 and T-6. The final lateral displacement is a PDF resulting from the four measurements between the mentioned piercing points. (b) Position of the paleochannel D's right margin in one of T-2 walls. Its orientation inferred from both trench walls is projected onto the fault (N_1-AMF). (c) Geometry of the paleochannel D in the photomosaic of T-6. Note that the position of the deepest exposure of the paleochannel is assumed as the northeasternmost position of the thalweg. Hence, its position could actually be more toward the SW implying a smaller lateral offset.

6.1. Individual Branch Slip Rates

6.1.1. N_1-AMF (La Tercia Site)

For the N_1-AMF at the La Tercia site, the strike slip rate is computed using the incision of paleochannel D as a marker. Although its age cannot be constrained with dates at this site, we infer its age based on stratigraphic

Table 3
Vertical Throw, Strike Slip, and Net Slip Rates of the Trenches

Time period	Marker used	Vertical throw (m)		Vertical throw rate (mm/yr)		Strike slip (m)	Strike slip rate (mm/yr)	Net slip (m)	Net slip rate (mm/yr)
N_1-AMF									
76.8/42.6 ka-present	Unit D3 (paleochannel)	2° rake	20° rake	2° rake	20° rake	$25.3^{+2.6}/_{-1.5}$	$0.59^{+0.06}/_{-0.04}$	$25.3^{+2.6}/_{-1.5}$	$0.59^{+0.06}/_{-0.04}$
		0.8–1 ±0.03	8.6–10 ± 0.4	$0.02^{+0.02}/_{-0.01}$	$0.21^{+0.02}/_{-0.01}$				
N_{2b}-AMF									
76.8 ka-present	Unit 6.2	7.6 ± 0.7		0.10 ± 0.01		–	–	7.9 ± 0.7	0.10 ± 0.01
42.6 ka-present	Unit 4.2	4.3 ± 0.3		0.10 ± 0.01		–	–	4.5 ± 0.3	0.11 ± 0.01
35 ka-present	Unit 2.1	2.6 ± 0.2		0.07 ± 0.01		–	–	2.7 ± 0.2	0.08 ± 0.01
76.8–42.6 ka	Unit 6 to 4.2	3.3 ± 0.8		0.10 ± 0.03		–	–	3.4 ± 0.8	0.10 ± 0.03
42.6–39.6 ka	Unit 4.2 to 2.2	1.7 ± 0.4		0.56 ± 0.14		–	–	1.8 ± 0.4	0.59 ± 0.14
S-AMF									
73.4 ka-present	Unit N1	10.1 ± 0.3		$0.14^{+0.02}/_{-0.01}$		38.3 ± 1.2	$0.53^{+0.06}/_{-0.05}$	39.6 ± 1.2	$0.54^{+0.06}/_{-0.05}$
45.9 ka-present	Unit L2	8.9 ± 0.2		$0.20^{+0.02}/_{-0.01}$		33.7 ± 0.8	0.74 ± 0.06	34.9 ± 0.8	$0.76^{+0.07}/_{-0.06}$
31.2 ka-present	Unit J	6.8 ± 0.3		0.22 ± 0.02		25.8 ± 1.2	$0.83^{+0.09}/_{-0.07}$	26.7 ± 1.2	$0.86^{+0.09}/_{-0.08}$
16.7/15.2 ka-present	Unit B	4.3 ± 0.3		$0.27^{+0.03}/_{-0.02}$		$16.3^{+2.7}/_{-0.3}$	$1.01^{+0.15}/_{-0.10}$	$16.9^{+2.7}/_{-0.3}$	$1.05^{+0.15}/_{-0.10}$
73.4–45.9 ka	Unit N1 to L2	1.2 ± 0.4		0.05 ± 0.02		4.6 ± 1.4	$0.18^{+0.09}/_{-0.06}$	4.7 ± 1.4	$0.19^{+0.09}/_{-0.06}$
45.9–31.2 ka	Unit L2 to J	2.1 ± 0.4		$0.15^{+0.04}/_{-0.03}$		7.9 ± 1.4	$0.55^{+0.14}/_{-0.11}$	8.2 ± 1.4	$0.57^{+0.15}/_{-0.12}$
31.2–21.7 ka	Unit J to I	2.5 ± 0.4		$0.30^{+0.14}/_{-0.07}$		9.5 ± 1.1	$1.15^{+0.50}/_{-0.25}$	9.8 ± 1.2	$1.18^{+0.54}/_{-0.30}$
F-AMF									
18.1 ka-present	Unit O	5.2 ± 0.1		0.29 ± 0.02		–	–	15.2 ± 0.3	0.84 ± 0.05
8.5 ka-present	Unit B (top)	2.2 ± 0.2		0.26 ± 0.02		–	–	6.4 ± 0.6	0.75 ± 0.07
18–9.5 ka	Unit O to B (base)	3.0 ± 0.2		$0.35^{+0.05}/_{-0.04}$		–	–	8.8 ± 0.7	$1.03^{+0.16}/_{-0.13}$

Note. The slip rates are provided for different time periods in N_1-AMF, N_{2b}-AMF (T-1), S-AMF (T-16) and F-AMF (T-3). The time periods used are marked by the numerical ages of the bracketing marker units (second column). All values correspond to the median and 1σ intervals. Note that some slip rate values in S-AMF show larger uncertainties due to the error propagation of the slip. Blank fields mean "undetermined."

comparison with units at the El Roser site. Paleochannel D is postdated by unit C2 in T-2 (32.6 ± 0.3 to 34.4 ± 0.1 ka; Figure 7) and predated by unit Rg, whose age is unknown. At the El Roser, units 2.1–2.2 have similar sedimentological characteristics as unit C2 at the La Tercia, and also ages in the same range (35.0 ± 0.2 and 39.6 ± 0.2 ka, respectively). Hence, we correlate these strata as likely having been deposited during the same phase of aggradation. In this manner, the underlying alluvial units 3.1 to 6.2 can be correlated by stratigraphic correspondence to unit D, with an age range of a minimum 42.6 ± 0.2 ka (base of unit 4.2) to a maximum 76.8 ± 5.6 ka (base of unit 6.2). Considering the offset of the paleochannel D ($25.3^{+2.6}/_{-1.5}$ m) and the mentioned estimated dates, this yields a strike slip rate between $0.59^{+0.06}/_{-0.04}$ mm/yr (mean and 1σ interval) and $0.33^{+0.04}/_{-0.03}$ mm/yr, respectively. Accounting for the rake variability (2°–20°), such strike slip rates translate into a minimum net slip rate of 0.33–$0.35^{+0.04}/_{-0.03}$ mm/yr (past 76.8 ± 5.6 ka) and a maximum between 0.59 and $0.62^{+0.06}/_{-0.04}$ mm/yr (past 42.6 ± 0.2 ka). In the same manner, the vertical throw rates range widely from 0.02 to $0.21^{+0.02}/_{-0.01}$ mm/yr (Table 3).

It should be noted that the age of the incision could be older than the infill deposits of paleochannel D and, therefore, because the channel incision is the feature used as the offset marker, the calculated slip rate range is a maximum. Similarly, the offset of paleochannel D is also a maximum (see Section 5.3.2).

6.1.2. N_{2b}-AMF (El Roser Site)

The vertical throw rates are computed for different time periods, highlighting a slight decrease in the mean uplift values toward recent times; the mean long-term values (past 76.8 ± 5.6 ka; 0.10 ± 0.01 mm/yr) are higher than the mean short-term rates (past 35.0 ± 0.2 ka; 0.07 ± 0.01 mm/yr) (Table 3). If we analyze the periods in-between,

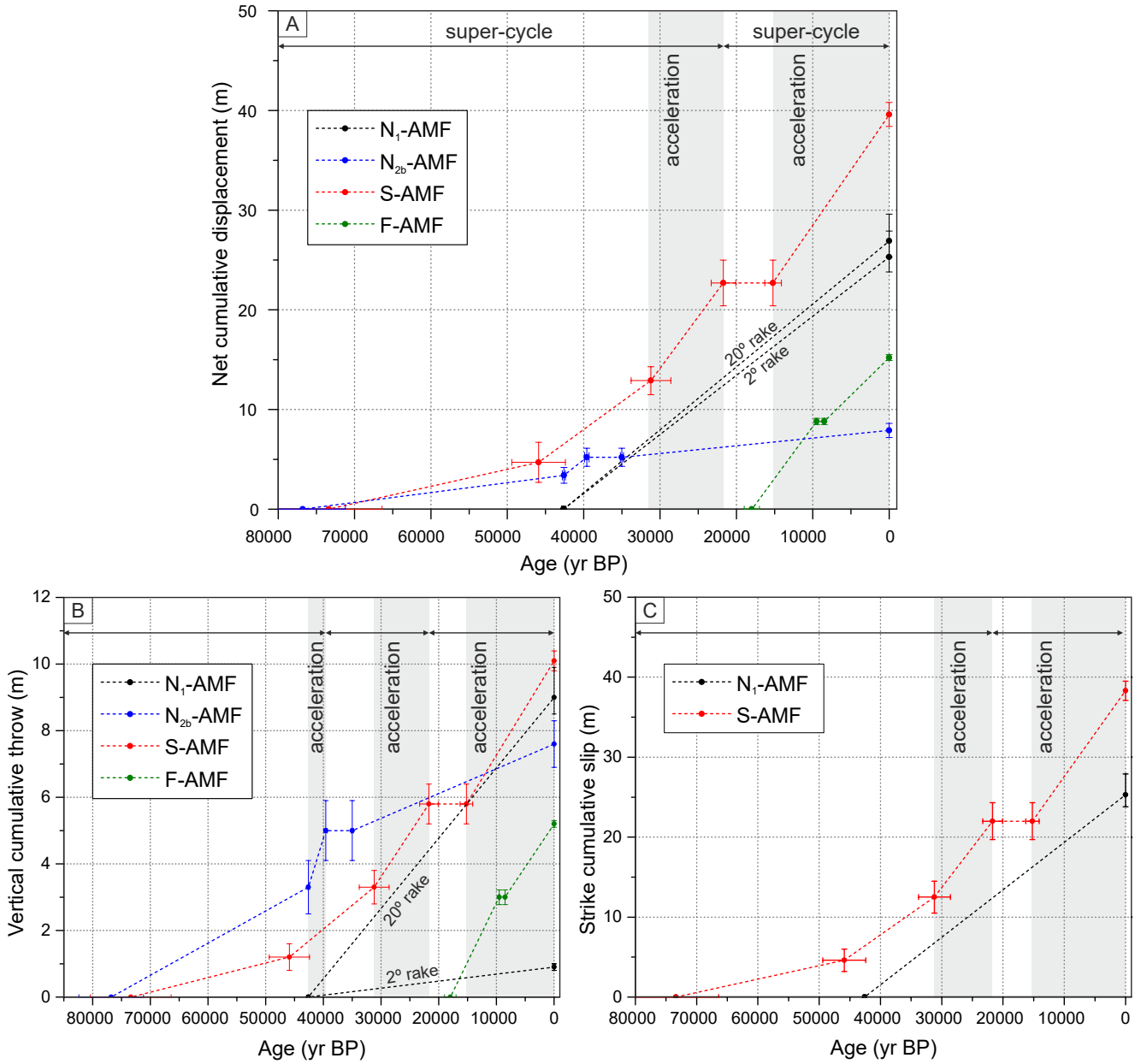

Figure 11. Cumulative slips as a function of time for the (a) net, (b) vertical and (b) strike components for each of the fault branches studied. For the net slip and vertical throw, the comparison between branches is only reliable for the last ~18 ka because the record available in the F-AMF controls this period. The strike slip is reliable for the last ~42 ka controlled by N_1-AMF. The slope of the curves that link the different data points in each branch represents the slip rate between time periods (Table 3), with higher slopes representing higher slip rates. Note that for the N_1-AMF two curves are provided to represent the uncertainty linked to the fault rake. Ages are extracted from numerical dates of the units in the trenches (Table 1), and cumulative slips are inferred from the values in Table 2. Gray bands represent periods of slip rate acceleration with respect to periods of decreased slip rates (white bands).

we observe that this decrease is not progressive but was preceded by a drastic increase between 42.6 ± 0.2 and 39.6 ± 0.2 ka (0.56 ± 0.14 mm/yr) (Figure 11b). Remarkably, we infer that there was no displacement on the fault during the deposition of units 2.2 and 2.1 because they are equally deformed, which is interpreted as a "no-slip" period in this specific fault branch. This is and evidence of its seismogenic behavior, although the possibility of coseismic ruptures in other parallel fault branches cannot be discarded. The throw rates are minimums because the structural modeling provides minimum vertical displacements, especially for older units where the complete structure is not visible in the trench (e.g., unit 6; Figure 9). Similarly, the net slip rates here lack the estimation of the strike slip, further highlighting that such estimations are minimums.

6.1.3. S-AMF (El Saltador Site)

The vertical throw rates are computed in four age markers for both long-term (unit N1; 73.4 ± 7.0 ka) and short-term (units L2, J and B; 45.9 ± 3.5, 31.2 ± 2.6, and 15.2 ± 1.1 ka, respectively). Higher slip rates are identified if shorter periods are considered, with a maximum vertical slip rate of $0.27^{+0.03}/_{-0.02}$ mm/yr for the past 16.7 ± 0.2 to 15.2 ± 1.1 ka (Table 3). When analyzing this increase in rate, we recognize that it was achieved in two pulses, a smaller one of $0.15^{+0.04}/_{-0.03}$ mm/yr between 45.9 ± 3.5 to 31.2 ± 2.6 ka, and a larger one of $0.30^{+0.14}/_{-0.07}$ mm/yr between 31.2 ± 2.6 to 21.7 ± 1.6 ka (Figure 11b). As with the N_{2b}-AMF, the lack of apparent deformation between 21.7 ± 1.6 ka (unit I) and 15.2 ± 1.1 ka (unit B) is interpreted to indicate a quiescence period.

The strike slip rates depict the same temporal variation patterns as the vertical rates, but they are much higher due to the ∼14.8° rake of the S-AMF (Figure 11c). Here we better constrain the age of unit D than published in Ferrater et al. (2016) because of an additional date in unit E (16.7 ± 0.2 ka; T16-OSL-3), which is stratigraphically closer to unit D (Figure 8). The minimum age of D is defined by overlying unit B on top (15.2 ± 1.1 ka). This new age constraint yields a strike slip rate of $1.01^{+0.15}/_{-0.10}$ since 16.7 ± 0.2 to 15.2 ± 1.1 ka, consistent with but slightly higher than the 0.9 ± 0.1 mm/yr documented by Ferrater et al. (2016) (past 15.2 ± 1.1 to 21.9–22.3 ka).

The resulting net slip rates are the largest out of all the analyzed sites (Table 3), consistent with the most marked geomorphological expression of the branch.

6.1.4. F-AMF (La Hoya Site)

The F-AMF branch at the La Hoya depicts the most recent activity of the transect (Late Pleistocene to Early Holocene). The vertical throw rates are nearly identical for the two dated markers in T-3: 0.28 ± 0.02 mm/yr since 18 ± 1 ka (unit O) and 0.26 ± 0.02 mm/yr since 8.53 ± 0.04 ka (youngest age of unit B). Likewise, the net slip rates show the same patterns but with much higher values due to the low angle dip of the fault, requiring more shortening to achieve the same vertical displacements than high angle faults. The age of the last deformation can only be estimated posterior to 8.53 ± 0.04 ka due to the lack of dates in unit A (Figure 8), but could be historical given that this unit corresponds to modern La Salud Creek deposits.

6.2. Summed Slip Rates for the Transect

We provide summed vertical, lateral, and net slip rate values for the four branches analyzed across the transect considering that all branches link at depth. Because the age constraints differ from one site to another, we use markers with similar ages to ensure better comparison. The age reference for the past 18 ± 1 to 15.2 ± 1.1 ka is selected as the common and most reliable age period to compute the total slip rates across all branches, assuming that the slip rate has remained constant along the N_1-AMF and N_{2b}-AMF for the past 42.6 ± 0.2 to 76.8 ± 5.6 ka and 35.0 ± 0.2 ka, respectively. The average dip of the at-depth fault plane considered to compute the total slip rate is 70°, based on MT data by Martí et al., 2020 (Equation S4 of the extended methods in Supporting Information S1).

The total net slip rate of the transect ranges from $1.35^{+0.15}/_{-0.10}$ to $1.63^{+0.16}/_{-0.11}$ mm/yr for the four fault branches since 18 ± 1 to 15.2 ± 1.1 ka. This value comes from a total vertical throw rate between $0.11^{+0.04}/_{-0.03}$ and $0.31^{+0.04}/_{-0.03}$ mm/yr, and a strike slip rate between $1.34^{+0.16}/_{-0.10}$ and $1.60^{+0.16}/_{-0.11}$ mm/yr. Note that the total throw value results from subtracting the rates of S-AMF and F-AMF (because they have opposed dip directions) and adding the residual to the N_{2b}-AMF and N_1-AMF.

7. Discussion

7.1. Structural and Tectonic Characterization of the Alhama de Murcia Fault

The Lorca-Totana segment is composed of five sub-parallel branches that accommodate the overall transpression in a complex fault zone. These branches are estimated to link at depth, although the geometry of such a junction is still unresolved due to the lack of deep geophysical data. We suggest that the structural model of Figure 2b based on surface data, which is similar to the one proposed by Martínez-Díaz, Masana, and Ortuño (2012) and represents a positive flower structure typical of strike slip systems (e.g., Sylvester, 1988). The net slip rate vector decomposition reflects a predominant role of the lateral component in the transect since 18 ± 1 to 15.2 ± 1.1 ka,

even more considering that the strike slip is unknown in the N_2-AMF push-up. In fact, from the vertical and strike slip components of the slip rate, a strike slip predominant rake between 5° and 12° is inferred for the segment (using Equation S3 in Supporting Information S1). In this respect, the vertical component could result mainly from the extrusion of the tectonic blocks under the transpressive regime, especially because the more perpendicular orientation of the Lorca-Totana segment with respect to the Africa-Eurasia convergence (323° ± 1.8°; Argus et al., 2011) generates a complex restraining bend in a positive flower structure. Most importantly, this vertical component could be even smaller if the unstudied branch (N_{2a}-AMF) is accounted for, because its vertical rates should be subtracted from the N_{2b}-AMF as part of the same push-up. Similarly, in this setting, the strike slip component could be amplified by horizontal block extrusion. The findings by Alonso-Henar et al. (2020) in the Góñar-Lorca segment near Lorca support this model; the authors identify a clear strain partitioning in the fault zone and shear-related vertical extrusion of the fault gouge in the northernmost branch (equivalent to the N_1-AMF).

Previous studies have suggested a structural control of preexisting Miocene extensional faults in the development of the active transpressive structure of the AMF, for instance at the NE end of the fault (e.g., Herrero-Barbero et al., 2020). Up until the Late Miocene, these faults bounded major sedimentary basins located NW of the modern AMF trace (i.e., Lorca and Fortuna basins; Figure 1c), which then inverted into oblique-reverse faults forming the related thrust-fold ranges of the Las Estancias, La Tercia and Espuña (Martínez-Díaz, 1998; Meijninger & Vissers, 2006; Montenat et al., 1987). In the transect, the northernmost branch (N_1-AMF) is likely the clearest expression of such an inherited structure as it constitutes the wide tectonic boundary between the SE margin of Lorca basin and the La Tercia range on the one hand, and the Guadalentín sector on the other hand (Figure 1b). Despite being the main structural limit, additional evidence for tectonic inheritance in this sector of the fault is not yet clear given the complexity of the deformation zone. Along this line, microstructural studies have shown no evidence of inherited fabrics representing stress fields prior to the current regime (see references in Alonso-Henar et al., 2021), so more work is needed in this aspect.

The current nearly pure strike slip motion of the N_1-AMF contrasts with the prominent range that this fault limits. This suggests a shift in the mountain front kinematics, from a strong reverse component during the early neotectonic basin-inversion phase, to strike slip at least during the Late Quaternary record (from Cg unit; past ~200 ka). Accordingly, most of the vertical component of the system seems to be currently accommodated along the frontal pressure ridge (Figure 11b). Martínez-Díaz (2002) proposed that the variations in the kinematics of the Lorca-Totana segment over time can be related to phenomena such as static stress transfer (interaction) between fault blocks, horizontal block motion in the fault zone, differential uplift rates in the hanging wall, among other processes that should be investigated. These observations however contrast with the strong reverse kinematics of the 2011 Lorca earthquake (39° rake; Martínez-Díaz, Bejar-Pizarro, et al., 2012) at the equivalent northern fault zone, which may suggest that the behavior of the fault at depth is different than what we infer from surface data.

The other fault branches show less cumulative activity, not representing large block boundaries as observed for the N_1-AMF. This might suggest that some of these fault branches have less of a relationship with this inherited structure and thus could have formed later to accommodate the neotectonic kinematics. The models by Sibson and Ghisetti (2018) help to back up this idea in the area: on the one hand, fault refractions due to propagation of basement-reactivated faults up to the sedimentary covers; on the other hand the formation of low-angle shortcut faults due to the inversion of inherited structures misoriented with respect to the regional stress field. The former model induces the formation of new lower angle (Andersonian) thrust and pop-up structures, coherent with the configurations of the N_2-AMF or the frontal pressure ridge. For instance, Herrero-Barbero et al. (2020) have interpreted refraction as the cause of dip decrease at the surface in the NE tip of the AMF. The latter model could also be the explanation for a frontal thrust in the transect (F-AMF) (Figure 2b). Along this line of reasoning, subsurface data is important to unveil the relationships of the different fault branches at depth and their role related to preexisting structures.

7.2. Temporal Variability of Slip Rates and Insights on Tectonic Evolution

7.2.1. Short-Term Slip Rates

In this work, we include three additional fault branches of the Lorca-Totana segment with respect to a previous estimation of the slip rate in the area (Ferrater et al., 2016). We first discuss here the short-term slip rates for

the past 18 ± 1–15.2 ± 1.1 ka because the period is the one with a deformation record for all the studied fault branches. The short-term net slip rate obtained for the entire fault zone ($1.35^{+0.15}/_{0.10}$–$1.63^{+0.16}/_{0.11}$ mm/yr since 18 ± 1–15.2 ± 1.1 ka) is 1.5 to nearly twice the rate determined from the previous study (0.9 ± 0.1 mm/yr; past 21.9–22.3 to 15.2 ± 1.1 ka), which was only estimated from the S-AMF at the El Saltador site. This highlights the importance of accounting for displacement across the entire deformation zone to develop a more reliable characterization of active faults.

The analysis of the slip rates of each branch reveals that the S-AMF accommodates the largest part of the lateral (60%–75%) and net slip since ∼15 ka, which is consistent with its prominent geomorphological expression. This percentage, however, is a maximum because the contribution to the strike slip of other branches in the segment is not yet determined. Arguably, the push-up context and high-angle dips of the N_2-AMF suggest that a strike slip component is likely present in either or both bounding fault strands, and therefore that the strike slip rate of the system obtained here is a minimum. Contrarily, the N_1-AMF accommodates the remaining 25%–40%, which is also a maximum since (a) the younger age assigned to the reference paleochannel D is a minimum, and (b) its displacement is a maximum estimate.

From the vertical component we observe that the S-AMF and F-AMF present the higher vertical throw rates, although they counteract each other in terms of overall uplift due to their opposite dips. Both branches show nearly identical rates for the past 18 ± 1–15.2 ± 1.1 ka (Table 3), coherent with a pressure ridge context where the tectonic block in-between is uplifted by extrusion due to the strike slip motion of the bounding faults at depth. Also, the slightly higher vertical throw rates of F-AMF explain why the El Saltador fan is uplifted with respect to the Guadalentín Depression. Likewise, the horizontal slip is partitioned between both branches with similar rates (Table 3): S-AMF absorbs the strike slip component while the F-AMF the heave (i.e., the shortening in the dip direction of the fault). In this setting, simultaneous ruptures between S-AMF and F-AMF are expectable.

The N_{2b}-AMF is the other remarkable branch with a vertical component, although its smaller rates suggest a minor presence of uplift in the northern sector of the transect. Such rates in a relative short-term range are in agreement with the $0.087^{+0.003}/_{-0.009}$ mm/yr relative long-term rate (past 198–26 ka) inferred by Martínez-Díaz and Hernández-Enrile (2001) for the equivalent branch at the La Carraclaca site, NE of Lorca (see location in Figure 2b). As with the S-AMF and F-AMF, the push-up context of this branch with respect to its antithetic strand (N_{2a}-AMF; Figure 2b) suggests that their vertical throw rates counteract. This points out that, when considering this unstudied branch, the total vertical throw rate of the transect in the short-term could be lower than the rate estimated here (0.11–$0.31^{+0.04}/_{-0.03}$ mm/yr), further supporting that the vertical component is caused by the block movement within a left-lateral fault zone.

Aside from the improvements obtained by multi-site analysis, the excavation of T-16 across the S-AMF allows for a better understanding of the fault structure and related vertical throw rates. Our rate is ∼2.6 times higher than that of Ferrater et al. (2016) (0.1 mm/yr) because we account for the depositional alluvial slope (3.9°) as a reference frame from which to measure the vertical throws (Figure 9), while Ferrater et al. (2016) considered the horizontal. Given that the folding structure of S-AMF grows to the NW, the estimated vertical throws are higher if the natural SE-descending slope is considered.

7.2.1.1. Comparison With Geodetic Data

The geological short-term slip rates provide further evidence that the AMF is one of the most prominent faults in the EBSZ and plays a major role in the deformation rates caused by the Eurasia-Africa convergence (4–6 mm/yr; DeMets et al., 2015). According to the geodetic data by Echeverria et al. (2013) and Borque et al. (2019), the EBSZ accommodates about 25% (0.6–0.8 ± 0.4 mm/yr; N315° direction) of the convergence in the Eastern Betic Cordillera and Mediterranean margin (1.6–2.7 mm/yr; Serpelloni et al., 2007). From this convergence, Echeverria et al. (2013) calculate an oblique-reverse horizontal rate of 1.5 ± 0.3 mm/yr (N12° azimuth) across the Guadalentín Depression. This value accounts for both the AMF and Palomares Fault (PF), as the contribution of each cannot be resolved from the geodetic network layout. If the geological slip rates obtained here match the geodetic values, the AMF would be accommodating all the slip rate across the Guadalentín Depression with practically no contribution from the PF. Consistently, previous authors (e.g., Ferrater et al., 2017) have already identified such predominancy of the AMF and low slip-rate of the PF in the Guadalentín area, based also on the lack of seismicity of the latter fault.

Comparing geodetic estimates of rate with our geological slip rates might lead to discrepancies that may reflect mainly differences between on-fault and off-fault deformation. Moreover, the comparison should be approached cautiously because, unlike the geodetic strain rate, geological rates are averaged over thousands or tens of thousands of years and may not reflect the current elastic strain accumulation of the fault. In our case, further complexity is introduced from: (a) the fact that the slip rates show noticeable fluctuations over time (Figure 11) and (b) the way that the estimated total slip rates are based on sums that do not necessarily represent correlative ages from branch to branch; for instance, the shorter-term slip rate for the N_1-AMF is at minimum for the past 42.6 ± 0.2 ka, whereas the rate for the S-AMF is for the past 15.2 ± 1.1 ka.

7.2.2. Slip Rate Variability Over Time and Tectonic Implications

Fault slip rate is a crucial parameter for fault-based seismic hazard as it controls the rate of earthquakes and the resulting hazard levels exceeded in a time frame (e.g., Field et al., 2014; Youngs & Coppersmith, 1985). Identifying its variations is critical as the selected periods highly impact the average slip rates used for probabilistic seismic hazard analyses (PSHA). We identify slip rate variations over time in three fault branches, occurring in different patterns depending on the branch (Figure 11). A transposition of the vertical throw rate toward the frontal branch is also detected, as discussed below.

The S-AMF has the strongest control in the net slip rate fluctuations for the past 73.4 ± 7.0 ka according to the analysis in Figure 11, which is coherent with its predominant footprint at the surface throughout the area. It should be noted, however, that the time frames of the geological records are not coincident between branches, so that the last 18 ± 1–15.1 ± 1.1 ka is the only period with deformational records for all of them. Because of this, and because both the S-AMF and F-AMF have similar contributions to the formation of the pressure ridge during the last ∼18 ka, we suspect that the F-AMF could have had the same contribution as the S-AMF did earlier. As for the other branches, the N_{2b}-AMF shows a minor contribution to the net slip evolution with a slight decrease in the vertical throw after 40 ka. In contrast, the lack of age control in the sediments at the La Tercia site hinders the development of the evolution of the N_1-AMF.

For the Upper Pleistocene-Holocene record of the transect, the slip rate evolution shows cyclic patterns characterized by long periods of lower to no displacement, alternating with short periods (3–9 kyr) of higher slip. Several causes need to be considered to explain these variations, from the inherent fault behavior (non-characteristic ruptures, aperiodic behavior or stress variations within the AMF) to changes affecting the whole EBSZ or even the plate tectonic boundary between Africa and Eurasia.

A simple explanation to the slip rate changes could be that earthquake ruptures in the AMF do not follow a characteristic model. This means that, depending on the seismic cycle considered, the studied section could be alternatively within a larger (central) slip area of the rupture and causing larger offset differences between sedimentary markers on the one hand, or at its tips and thus causing smaller offsets on the other hand. Contrarily, assuming that the ruptures are, in general terms, characteristic, at least at a section scale, the discussion could be open to other causes such as the existence of super-cycles or local/regional changes in stress.

Slip rate change patterns over time have been previously identified in other settings such as the Wasatch Fault (Friedrich et al., 2003), the White Mountain Fault (Kirby et al., 2006) or the Garlock Fault (Dolan et al., 2016). These have been related to super-cyclic variations in the strain rates over time that follow the same increase-decrease alternations. If this was the case, two main super-cycles can be identified in the net and strike slip components, driven by the activity of the S-AMF (Figures 11a and 11c), while three such cycles can be identified for the vertical throw due to observations on the N_{2b}-AMF (Figure 11b). The number of cycles is a minimum because (a) we do not have data on the variations for periods prior to 18 ka for the F-AMF, nor do we have the resolution for the N_1-AMF, and (b) because the sedimentary sequence in all trenches comprises periods without deposition (i.e., deformation record) that are potentially masking fluctuations. The variations in the vertical throw are most interesting because they depict a slight decrease in the north (N_{2b}-AMF) since ∼40 ka, which translates into an increase in the activity along the S-AMF for the same period (Figure 11b). As explained, for the past 18 ± 1–15.1 ± 1.1 ka, the vertical rates are dominated by both the S-AMF and F-AMF, while these are practically negligible along the northern part of the fault zone. This evolution since 40 ka suggests a southwards transposition of the uplift in the transect, consistent with the evolutive models of active mountain ranges where the youngest activity is progressively recorded in the forelands (e.g., Vergés et al., 2002). The decreased uplift in the north is also consistent with the (a) observed abandonment of the alluvial deposition at the upper parts of

the El Saltador fan after 39.6 ± 0.2 ka, and (b) the subsequent migration of the alluvial systems toward the frontal zone, as first described by Silva et al. (1992) and evidenced by the fluvial entrenchment NW of the F-AMF.

Super-cyclic patterns in the slip rate at the EBSZ are not restricted to the AMF but have also been identified along the NE segment of the Carrascoy Fault (CAF) by Martín-Banda et al. (2021). For the first time in paleoseismic studies in the Iberian Peninsula, we can compare with a minimum of resolution, the slip rate variations over time of two neighboring faults. Interestingly, the most prominent slip rate acceleration in the CAF, between 34 and 28 ka, shows a good correlation in time and duration with the most prominent acceleration along the S-AMF (31–22 ka). We consider that this could indicate synchronous activity among faults, unprecedented in SE Spain, although the mechanisms for it have been ignored so far and need to be investigated. Also, it should be noted that the correlation is only based on two discrete observations from two separate faults; therefore, more data is probably needed across the fault system to establish more robust and confident statements about fault behavior. Demonstrating synchronous activity in the EBSZ is strongly significant for the tectonic understanding of the area and for the earthquake rate modeling in future SHA.

Strain rates on faults are usually considered as constant between earthquake cycles, either because the resolution of geological data is insufficient to depict variations (scarcity of markers; e.g., Kirby et al., 2006) or because the data comes from GNSS, which covers too short of a time span. Our slip rate analysis suggests that this constant strain model is likely not suitable for the AMF, at least for some of the branches considered in this study, albeit the driving forces of such variations are yet to be understood. Dolan et al. (2016), summarizes three possible mechanisms proposed in the literature: (a) weakening and strengthening of the fault zone in the crust leading to earthquake clustering or gaps, respectively; (b) stress changes over time in the fault system; (c) rarely, changes in the plate motions driving fault activity.

In terms of earthquake clustering, the available data does not have enough resolution to relate deformation increments to clusters or to a large slipping event. For instance, the slip increment of 31–22 ka is exclusively determined by the deformation difference between the consecutive dated units J and I in T-16 (Figure 9). Because there is no record in between these units, estimating whether or not such deformation was achieved by one or more than one earthquake is impossible at this site. Despite this, clustering behavior in the AMF is already deduced from the paleoearthquake chronologies of Ferrater et al. (2016) at the El Saltador site, with groups of events occurring in short periods of time, while others are separated by larger time spans. In this sense, refined chronologies for the different sites studied that are currently ongoing will further help to discern earthquake clustering behavior in the AMF.

Concerning stress field changes over time, few data are available on the role of stress in the evolution of fault activity at the EBSZ. Martínez-Díaz (2002) identified stress orientation changes of the AMF since the Upper Miocene and related them to phenomena such as dynamic interaction between fault strands. Although these changes were not directly implicated as the cause for strain rate variations in the system, they could be one explanation. Another possibility is that stress changes occurred at a larger scale, related to static and/or dynamic interaction between the AMF and other EBSZ faults. The recent work by Herrero-Barbero et al. (2021) suggested that fault interaction is a possibility in the EBSZ by means of earthquake rupture propagation across fault sections. This study used the RSQSim code (Dieterich & Richards-Dinger, 2010), which is a physics-based earthquake simulator that allows to model earthquake occurrences in time and space, while also considering the physical characteristics of earthquake ruptures at the fault system scale. Specifically, for the AMF, the authors remark that the fault is capable of transferring slip to neighboring faults across the Guadalentín Depression, such as to the Los Tollos Fault. If correct, fault interaction in terms of stress transfer (static and/or dynamic) could be a plausible cause for the time-coincident slip rate increments in both the AMF and CAF, although the rupture compatibility analysis between them is pending.

Regarding changes in the plate motions, these are an unlikely cause for the observed slip rate variations because, probably, the time windows analyzed in the AMF are too short (<100 ka) to capture significant shifts in the plate motions. For instance, studies such as Calais et al. (2003) have suggested that the convergence direction and rate between Eurasia and Africa have changed progressively since ∼3 Ma, becoming more oblique and slower. However, these changes usually encompass the million-year time scale, in contrast with the more rapid variations documented for the AMF which are thousands to tens of thousands of years long. Martínez-Díaz (2002) proposes that the kinematic changes of the AMF are compatible with a single regional stress field (NNW-SSE Eurasia-Africa convergence) if phenomena such as fault interaction and relative movements between fault-bounded blocks are

accounted for (constriction and vertical extrusion would be results of this). Consequently, we infer that the slip rate changes are also compatible with a constant regional stress field, considering the potential role of fault interaction in slip and strain rate variability.

In summary, our preferred hypotheses to explain the observed slip rate variability in the AMF are related to fault interaction stress changes, and earthquake clustering, both of which should be further investigated in the future.

7.3. Significance for the Seismic Hazard Assessment and Main Limitations

In general terms, this study proves that multi-site paleoseismic analysis is a useful approach to improve the reliability of paleoseismic parameters in active faults, compared to single-site studies. Low to moderate strain regions particularly benefit from such analyses, especially when the deformation is commonly distributed in broad and complex fault zones, because the evidence of tectonic activity is more affected (obliterated) by surface phenomena such as erosion and anthropization. The case presented here might be useful not only for the context of SE Spain but for other low to moderate strain rate regions worldwide that aim to characterize fault activity.

We state that the geological slip rates of the AMF over the last 15–18 ka are almost twice than the previously determined (0.9 ± 0.1 mm/yr; Ferrater et al., 2016), which suggest that an update of previous fault-based PSHAs is likely needed (e.g., Gómez-Novell et al., 2020; Rivas-Medina et al., 2018). In such studies, the AMF is one of the faults that contributes the most to the hazard levels (PGA) in SE Spain, also for standard return periods (e.g., 475 years). Hence, the new values would likely imply even higher hazard. Regularly updating hazard estimates should be standard practice, especially in areas such as SE Spain where the population levels and industrial development are high, and where the knowledge on faults has been developing rapidly over the past several years.

The results of this study highlight several limitations that need to be addressed and analyzed before their use in PSHA. The first limitation is the lack of data in one of the fault branches of the northern sector (N_{2a}-AMF), which underestimates the overall deformation and both the vertical and strike components of the displacement. In this regard, the overall poor characterization of the lateral component in the whole transect constitutes a remarkable limitation.

The lack of actual 3D trenching across all of the fault branches, except for the S-AMF, possibly contributes to the misestimation of the net displacement, and therefore the slip rate. On the one hand, the strike slip component related to the N_2-AMF push-up is undetermined here, which presumably leads to the underestimation of the net displacement in this fault strand. On the other hand, the strike slip component assigned to the N_1-AMF is a maximum value, as parallel trenching is lacking across the SE block of the fault (Figure 10), which might lead to an overestimate of the total net slip. Arguably, it should also be noted that there is a significant amount of deformation in the transect absorbed in bulk between fault branches at the surface (folding, etc.) and therefore, this component of the strike slip is not captured in our study (Figure 2).

Another limitation linked to the previous one is the potential inclusion of an apparent component to the vertical slip estimates. In strike slip faults, the lateral motion can result in apparent vertical separations of the stratigraphic units that can lead to errors in the vertical throw measurements, especially in alluvial environments where unit contacts have irregular geometries. The quantification of this effect, although difficult, we estimate it to be small here because, at all sites, the measured vertical throws are stratigraphically coherent and consistent throughout all trench walls analyzed.

Lastly, albeit one of the most important limitations, concerns the poor age control of parts of the stratigraphic sequences. First, the presence of large depositional gaps (see dates in Figures 7 and 8) due to the intrinsic intermittent deposition of the area results in difficulties where (a) correlative age periods between branches are needed to integrate slip rates more reliably and (b) capturing all slip rate fluctuations in the branches is unlikely (Figure 11). Second, the proximity of the sites to their respective sedimentary sources limits the capability of the luminescence techniques to yield useable dates, as the small transport distances can prevent the complete bleaching of all the quartz grains in the samples (e.g., Colarossi et al., 2015). This is the case of two samples in T-1 (Table 1), which result in OSL ages that are undetectable. Arguably, most of our samples might be affected by incomplete bleaching to some degree due to their depositional setting, hence older ages are likely obtained (i.e., underestimated slip rates). Third, the presence of predominantly coarse grained and clast-supported sediments

with highly irregular contacts increases the risk of mixing sediments from different units during the sampling process, especially for OSL, which could provide inadequate dates.

We encourage modelers to include the data presented here in fault-based PSHAs, but we also recall that such data should be used considering the aforementioned uncertainties. Most of them are mostly intrinsically linked to the paleoseismic recording and method; very local observations that are highly dependent on the characteristics of the specific site trenched. Thus, from our perspective, an important part of them could be aided by increasing the number of observations along the fault branches studied here. Extending the paleoseismic research in other sectors of the Lorca-Totana segment might fill in the information gaps identified in the current sites, especially considering that the alluvial sediments in the area are highly variable from site to site. If the deformation of more widespread and larger markers in the segment could be constrained and dated, the local or regional character of the slip rate variations could be verified and correlated between sites. Also, and based on the successful results in T-3 (F-AMF), we propose performing paleoseismic surveys at the bottom of the creeks in other fault branches to characterize their recent history (last ~40 kyr), which is not captured at the surface of the Q3 alluvial fans (e.g., northern Saltador fan). Such contributions would ultimately help to complete and refine the deformation history and parameters of the fault during the Late Pleistocene-Holocene period.

8. Conclusions

The Lorca-Totana segment of the AMF is a complex fault zone with at least five Quaternary active slip-partitioned branches that form lower order sub-structures likely linked at depth. From N to S these sub-order structures define the mountain front (N_1-AMF) and two push-up structures (N_{2a}-AMF–N_{2b}-AMF and S-AMF–F-AMF). The N_1-AMF and S-AMF are predominantly strike slip faults, while the N_{2a}-AMF–N_{2b}-AMF and F-AMF show strong dip-slip component. Previous studies only focused on characterizing the paleoseismic activity of one of the branches, potentially underestimating the entire fault-system slip rate. Here, we carry out a paleoseismic survey in four of the five fault branches, revealing that they all have been active during the Upper Pleistocene-Holocene period, generating metric-scale cumulative deformations on the sediments and the surfaces of the alluvial fans in the area.

We estimate a total net slip rate between $1.35^{+0.16}/_{-0.10}$ and $1.64^{+0.16}/_{-0.11}$ mm/yr (four fault branches) since 18 ± 1 to 15.2 ± 1.1 ka, based on fault-slip analysis combined with OSL and radiocarbon datings. This represents almost twice the previous estimated slip rate, which was solely based on data from a single branch and site, and demonstrates that accounting for complete structures yields more reliable fault characterizations. In detail, this value is decomposed in minimum lateral rates between $1.34^{+0.16}/_{-0.10}$ and $1.60^{+0.16}/_{-0.11}$ mm/yr and vertical rates between 0.11 and $0.31^{+0.04}/_{-0.03}$ mm/yr, respectively. The predominance of the lateral component suggests that the slip partitioning might be caused by the tectonic block re-adjustment under the overall strike slip motion of the fault, consistent with a flower-structure model of strike slip systems.

The slip rate analysis highlights a non-steady behavior of this parameter over time, following cyclic patterns of short accelerations and longer periods of quiescence mainly recorded by the S-AMF. Such fluctuations might be linked to non-characteristic ruptures or by changes in the strain rates of the system, potentially driven by stress field changes due to fault interaction or synchronicity, among other causes. The time coincidence of one significant acceleration in the AMF (31–22 ka) with another identified in the Carrascoy Fault by Martín-Banda et al. (2021) (34–28 ka) suggests this acceleration is a real process that deserves further regional investigation.

We emphasize that our paper constitutes a step forward to improve the characterization of the slip rates in the AMF and therefore motivates a reassessment of fault-based PSHA studies in the area, which have been demonstrated to be highly dependent on this parameter. Moreover, the multi-site approach followed in this study might serve as an example for other low-strain regions worldwide with complex fault zones. Despite this, two main limitations need to be assessed: on the one hand, the lack of paleoseismic data in one of the branches of the transect together with the absence of actual 3D trenching in three of the branches, might be underestimating the total slip rate of the AMF in this sector. On the other hand, the intermittent alluvial deposition of the area, together with the proximal alluvial fan context, makes it difficult to resolve reliable age controls of the stratigraphy and, therefore, the establishment of correlative time periods to integrate slip rates between sites. In this line, increasing the number of observations by extending paleoseismic studies to other parts of the fault is crucial to complete the deformation histories and slip rate characterization of the AMF.

Data Availability Statement

The data used to interpret the trenches and compute slip rate distributions in the study are available at Figshare via https://doi.org/10.6084/m9.figshare.20057069.v1 (Gómez-Novell et al., 2022) with free access under the license CC-BY 4.0. For the detailed geomorphological mapping we used a LiDAR-based high resolution digital terrain model (DTM) that was obtained in the frame of a previous project of the University of Barcelona (SHAKE project; CGL2011-30005-C02-01) funded by the former Spanish Ministry of Economy and Competitiveness. This DTM is available at Figshare via https://doi.org/10.6084/m9.figshare.19729597.v1 (SHAKE Working Group, 2022) with free access under the license CC-BY 4.0. This article and its supplement contain part of the results of the doctoral thesis of Octavi Gómez-Novell (Gómez-Novell, 2021), which is available at the repository Dipòsit UB of the University of Barcelona: http://hdl.handle.net/2445/183755 with free access.

Acknowledgments
This work has been supported by the "PREVENT" project (ref. CGL2015-66263-R) funded by the former Spanish of Economy, Industry and Competitiveness as well as by the "NSOURCES" project (ref. PID2020-119772RB-I00) funded by the Spanish Ministry of Science and Innovation. The work is part of the doctoral thesis of Octavi Gómez-Novell (Formación de Personal Investigador grant by the former Spanish of Economy, Industry and Competitiveness: ref. BES-2016-077048). We warmly thank all the colleagues that have attended and helped in the different trenching surveys, especially Robert López and Albert Baguer. We also thank Miren del Val Blanco, Alicia Medialdea and Ana Luísa Sebastião Rodrigues for the OSL dosimetry measurements in the field and fruitful discussions on numerical dates. Last but not least, we thank the detailed and very constructive contributions of Sam Haines and Paula Marques Figueiredo, both of which helped to improve the present manuscript.

References

Alguacil, G., Vidal, F., Navarro, M., García-Jerez, A., & Pérez-Muelas, J. (2014). Characterization of earthquake shaking severity in the town of Lorca during the May 11, 2011 event. *Bulletin of Earthquake Engineering*, *12*(5), 1889–1908. https://doi.org/10.1007/s10518-013-9475-y

Alonso-Henar, J., Fernández, C., & Martínez-Díaz, J. J. (2020). Application of the analytic model of general triclinic transpression with oblique extrusion to an active deformation zone: The Alhama de Murcia Fault (SE Iberian Peninsula). *Journal of Structural Geology*, *130*(February 2019), 103924. https://doi.org/10.1016/j.jsg.2019.103924

Alonso-Henar, J., Rodríguez-Escudero, E., Herrero-Barbero, P., Tsige, M., & Martínez-Díaz, J. J. (2021). Complete strain record of a highly asymmetric shear zone from fault core gouges to surface rupture of historical earthquakes in the Alhama de Murcia fault (SE Iberian Peninsula). *Lithosphere*, *2021*, 8876012. https://doi.org/10.2113/2021/8876012/5306774/8876012.pdf

AMC. (2001). Robust statistics: A method of coping with outliers. London, United Kingdom. In *Analitical methods comitee technical brief*. Royal Society of Chemistry.

Argus, D. F., Gordon, R. G., & DeMets, C. (2011). Geologically current motion of 56 plates relative to the no-net-rotation reference frame. *Geochemistry, Geophysics, Geosystems*, *12*(11), 1–13. https://doi.org/10.1029/2011GC003751

Borque, M. J., Sánchez-Alzola, A., Martin-Rojas, I., Alfaro, P., Molina, S., Rosa-Cintas, S., et al. (2019). How much Nubia-Eurasia convergence is accommodated by the NE end of the Eastern Betic Shear Zone (SE Spain)? Constraints from GPS velocities. *Tectonics*, *38*(5), 1824–1839. https://doi.org/10.1029/2018TC004970

Bousquet, J. C. (1979). Quaternary strike-slip faults in southeastern Spain. *Tectonophysics*, *52*(1–4), 277–286. https://doi.org/10.1016/B978-0-444-41783-1.50044-1

Calais, E., DeMets, C., & Nocquet, J.-M. (2003). Evidence for a post-3.16-Ma change in Nubia–Eurasia–North America plate motions? *Earth and Planetary Science Letters*, *216*(1–2), 81–92. https://doi.org/10.1016/S0012-821X(03)00482-5

Colarossi, D., Duller, G. A. T., Roberts, H. M., Tooth, S., & Lyons, R. (2015). Comparison of paired quartz OSL and feldspar post-IR IRSL dose distributions in poorly bleached fluvial sediments from South Africa. *Quaternary Geochronology*, *30*, 233–238. https://doi.org/10.1016/j.quageo.2015.02.015

DeMets, C., Iaffaldano, G., & Merkouriev, S. (2015). High-resolution Neogene and quaternary estimates of Nubia-Eurasia-North America plate motion. *Geophysical Journal International*, *203*(1), 416–427. https://doi.org/10.1093/gji/ggv277

Dieterich, J. H., & Richards-Dinger, K. B. (2010). Earthquake recurrence in simulated fault systems. *Pure and Applied Geophysics*, *167*(8–9), 1087–1104. https://doi.org/10.1007/s00024-010-0094-0

Dolan, J. F., Bowman, D. D., & Sammis, C. G. (2007). Long-range and long-term fault interactions in Southern California. *Geology*, *35*(9), 855–858. https://doi.org/10.1130/G23789A.1

Dolan, J. F., McAuliffe, L. J., Rhodes, E. J., McGill, S. F., & Zinke, R. (2016). Extreme multi-millennial slip rate variations on the Garlock fault, California: Strain super-cycles, potentially time-variable fault strength, and implications for system-level earthquake occurrence. *Earth and Planetary Science Letters*, *446*, 123–136. https://doi.org/10.1016/j.epsl.2016.04.011

DuRoss, C. B., Personius, S. F., Crone, A. J., Olig, S. S., & Lund, W. R. (2011). Integration of paleoseismic data from multiple sites to develop an objective earthquake chronology: Application to the Weber segment of the Wasatch fault zone, Utah. *Bulletin of the Seismological Society of America*, *101*(6), 2765–2781. https://doi.org/10.1785/0120110102

DuRoss, C. B., Zellman, M. S., Thackray, G. D., Briggs, R. W., Gold, R. D., & Mahan, S. A. (2021). Holocene paleoseismology of the steamboat mountain site: Evidence for full-length rupture of the Teton fault, Wyoming. *Bulletin of the Seismological Society of America*, *111*(1), 439–465. https://doi.org/10.1785/0120200212

Echeverria, A., Khazaradze, G., Asensio, E., Gárate, J., Dávila, J. M., & Suriñach, E. (2013). Crustal deformation in eastern Betics from CuaTeNeo GPS network. *Tectonophysics*, *608*, 600–612. https://doi.org/10.1016/j.tecto.2013.08.020

Echeverria, A., Khazaradze, G., Asensio, E., & Masana, E. (2015). Geodetic evidence for continuing tectonic activity of the Carboneras fault (SE Spain). *Tectonophysics*, *663*, 302–309. https://doi.org/10.1016/J.TECTO.2015.08.009

Ferrater, M. (2016). *Velocitat de desplaçament de la falla d'Alhama de Murcia (Bètiques Orientals); implicacions en el seu potencial sísmic* (Doctoral dissertation). Universitat de Barcelona. Retrieved from https://urldefense.com/v3/__http://hdl.handle.net/2445/107319__;!!N11eV2i-wtfs!vzBCpwogsI-EzYHDKKMP_Woff6qrapZ2OE_pEuSmheWRwIbm4zF7h3_gtTzJPqJC6SO7a0o1rPVLJmsaW81_yu_SDUDB$

Ferrater, M., Arrowsmith, R., & Masana, E. (2015). Lateral offset quality rating along low slip rate faults: Application to the Alhama de Murcia Fault (SE Iberian Peninsula). *Remote Sensing*, *7*(11), 14827–14852. https://doi.org/10.3390/rs71114827

Ferrater, M., Ortuño, M., Masana, E., Martínez-Díaz, J. J., Pallàs, R., Perea, H., et al. (2017). Lateral slip rate of Alhama de Murcia fault (SE Iberian Peninsula) based on a morphotectonic analysis: Comparison with paleoseismological data. *Quaternary International*, *451*, 87–100. https://doi.org/10.1016/j.quaint.2017.02.018

Ferrater, M., Ortuño, M., Masana, E., Pallàs, R., Perea, H., Baize, S., et al. (2016). Refining seismic parameters in low seismicity areas by 3D trenching: The Alhama de Murcia fault, SE Iberia. *Tectonophysics*, *680*, 122–128. https://doi.org/10.1016/j.tecto.2016.05.020

Field, E., Biasi, G. P., Bird, P., Dawson, T. E., Felzer, K. R., Jackson, D. D., et al. (2014). The uniform California earthquake rupture forecast, version 3 (UCERF3). *Bulletin of the Seismological Society of America*, *3*(104), 1122–1180. https://doi.org/10.3133/ofr20131165

Field, E. H., Biasi, G. P., Bird, P., Dawson, T. E., Felzer, K. R., Jackson, D. D., et al. (2015). Long-term time-dependent probabilities for the third Uniform California Earthquake Rupture Forecast (UCERF3). *Bulletin of the Seismological Society of America*, *105*(2), 511–543. https://doi.org/10.3133/fs20153009

Friedrich, A. M., Wernicke, B. P., Niemi, N. A., Bennett, R. A., & Davis, J. L. (2003). Comparison of geodetic and geologic data from the Wasatch region, Utah, and implications for the spectral character of Earth deformation at periods of 10 to 10 million years. *Journal of Geophysical Research*, *108*(B4), 2199. https://doi.org/10.1029/2001JB000682

Galbraith, R. F., & Roberts, R. G. (2012). Statistical aspects of equivalent dose and error calculation and display in OSL dating: An overview and some recommendations. *Quaternary Geochronology*, *11*, 1–27. https://doi.org/10.1016/j.quageo.2012.04.020

Gold, R. D., Cowgill, E., Arrowsmith, J. R., Chen, X., Sharp, W. D., Cooper, K. M., & Wang, X.-F. (2011). Faulted terrace risers place new constraints on the late Quaternary slip rate for the central Altyn Tagh fault, northwest Tibet. *The Geological Society of America Bulletin*, *123*(5–6), 958–978. https://doi.org/10.1130/B30207.1

Gómez-Novell, O. (2021). *Paleoseismic transect across the Alhama de Murcia Fault and implications of a fault-based seismic hazard assessment for the Eastern Betics* (Doctoral dissertation). Universitat de Barcelona. Retrieved from http://hdl.handle.net/2445/183755

Gómez-Novell, O., García-Mayordomo, J., Ortuño, M., Masana, E., & Chartier, T. (2020). Fault system-based probabilistic seismic hazard assessment of a moderate seismicity region: The eastern Betics shear zone (SE Spain). *Frontiers of Earth Science*, *8*(December), 579398. https://doi.org/10.3389/feart.2020.579398

Gómez-Novell, O., Ortuño, M., García-Mayordomo, J., Insua-Arévalo, J. M., Rockwell, T. K., Baize, S., et al. (2022). Improved geological slip rate estimations in the complex Alhama de Murcia Fault zone (SE Iberia) and its implications for fault behavior [Dataset]. Tectonics. http://dx.doi.org/10.6084/m9.figshare.20057069.v1

Herrero-Barbero, P., Álvarez-Gómez, J. A., Martínez-Díaz, J. J., & Klimowitz, J. (2020). Neogene Basin inversion and recent slip rate distribution of the northern termination of the Alhama de Murcia Fault (Eastern Betic Shear Zone, SE Spain). *Tectonics*, *39*(7), 1–25. https://doi.org/10.1029/2019TC005750

Herrero-Barbero, P., Álvarez-Gómez, J. A., Williams, C., Villamor, P., Insua-Arévalo, J. M., Alonso-Henar, J., & Martínez-Díaz, J. J. (2021). Physics-based earthquake simulations in slow-moving faults: A case study from the Eastern Betic Shear Zone (SE Iberian Peninsula). *Journal of Geophysical Research: Solid Earth*, *126*(5), e2020JB021133. https://doi.org/10.1029/2020jb021133

IGME. (2015). ZESIS: Base de Datos de Zonas Sismogénicas de la Península Ibérica y territorios de influencia para el cálculo de la peligrosidad sísmica en España [Database]. Retrieved from http://info.igme.es/zesis

IGME. (2022). QAFI v.4: Quaternary active faults database of Iberia [Database]. Retrieved from http://info.igme.es/qafi

IGN. (2011). *Serie terremoto NE Lorca (Murcia). (Technical report)*. Instituto Geográfico Nacional. Retrieved from http://www.ign.es

IGN-UPM. (2013). *Actualización de mapas de peligrosidad sísmica de España 2012*. Centro Nacional de Información Geográfica, Instituto Geográfico Nacional.

Insua-Arévalo, J. M., García-Mayordomo, J., Salazar, A. E., Rodríguez-Escudero, E., Martín-Banda, R., Álvarez-Gómez, J. A., et al. (2015). Paleoseismological evidence of Holocene activity of the Los Tollos fault (Murcia, SE Spain): A lately formed quaternary tectonic feature of the Eastern Betic Shear Zone. *Journal of Iberian Geology*, *41*(3), 333–350. https://doi.org/10.5209/rev_JIGE.2015.v41.n3.49948

Kirby, E., Burbank, D. W., Reheis, M., & Phillips, F. (2006). Temporal variations in slip rate of the White Mountain fault zone, eastern California. *Earth and Planetary Science Letters*, *248*(1–2), 168–185. https://doi.org/10.1016/j.epsl.2006.05.026

López-Comino, J. Á., Mancilla, F. D. L., Morales, J., & Stich, D. (2012). Rupture directivity of the 2011, M_w 5.2 Lorca earthquake (Spain). *Geophysical Research Letters*, *39*(3), 1–5. https://doi.org/10.1029/2011GL050498

Marín-Lechado, C., Roldán-García, F. J., Pineda-Velasco, A., Martínez-Zubieta, P., Rodero-Pérez, J., & Díaz-Pinto, G. (2011). Mapa Geológico Digital Continuo E 1:50000, Zonas Internas de las Cordilleras Béticas (Zona-2100). Retrieved from https://mapas.igme.es/gis/services/Cartografia_Geologica/IGME_MAGNA_50/MapServer/WMSServer

Martí, A., Queralt, P., Marcuello, A., Ledo, J., Rodríguez-Escudero, E., Martínez-Díaz, J. J., et al. (2020). Magnetotelluric characterization of the Alhama de Murcia Fault (Eastern Betics, Spain) and study of magnetotelluric interstation impedance inversion. *Earth Planets and Space*, *72*(1), 16. https://doi.org/10.1186/s40623-020-1143-2

Martín-Banda, R., García-Mayordomo, J., Insua-Arévalo, J. M., Salazar, A. E., Rodríguez-Escudero, E., Álvarez-Gómez, J. A., et al. (2015). New insights on the seismogenic potential of the Eastern Betic Shear Zone (SE Iberia): Quaternary activity and paleoseismicity of the SW segment of the Carrascoy Fault Zone. *Tectonics*, *35*(1), 55–75. https://doi.org/10.1002/2015TC003997

Martín-Banda, R., Insua-Arévalo, J. M., & García-Mayordomo, J. (2021). Slip rate variation during the last ~210 ka on a slow fault in a transpressive regime: The Carrascoy Fault (Eastern Betic Shear Zone, SE Spain). *Frontiers of Earth Science*, *8*(February), 1–21. https://doi.org/10.3389/feart.2020.599608

Martínez-Díaz, J. J. (1998). *Neotectónica y Tectónica Activa del Sector Centro-Occidental de la Región de Murcia y Sur de Almería (Cordillera Bética – España)* (Doctoral dissertation). Universidad Complutense de Madrid.

Martínez-Díaz, J. J. (2002). Stress field variation related to fault interaction in a reverse oblique-slip fault: The Alhama de Murcia fault, Betic Cordillera, Spain. *Tectonophysics*, *356*(4), 291–305. https://doi.org/10.1016/S0040-1951(02)00400-6

Martínez-Díaz, J. J., Alonso-Henar, J., Insua-Arévalo, J. M., Canora, C., García-Mayordomo, J., Rodríguez-Escudero, E., et al. (2018). Geological evidences of surface rupture related to a seventeenth century destructive earthquake in betic Cordillera (SE Spain): Constraining the seismic hazard of the Alhama de Murcia fault. *Journal of Iberian Geology*, *45*(1), 73–86. https://doi.org/10.1007/s41513-018-0082-2

Martínez-Díaz, J. J., Bejar-Pizarro, M., Álvarez-Gómez, J. A., Mancilla, F. D. L., Stich, D., Herrera, G., & Morales, J. (2012). Tectonic and seismic implications of an intersegment rupture. *Tectonophysics*, *546–547*, 28–37. https://doi.org/10.1016/j.tecto.2012.04.010

Martínez-Díaz, J. J., & Hernández-Enrile, J. L. (2001). Using travertine deformations to characterize paleoseismic activity along an active oblique-slip fault: The Alhama de Murcia fault (Betic Cordillera, Spain). *Acta Geologica Hispanica*, *36*(3–4), 297–313.

Martínez-Díaz, J. J., Masana, E., Hernández-Enrile, J. L., & Santanach, P. (2003). Effects of repeated paleoearthquakes on the Alhama de Murcia Fault (Betic Cordillera, Spain) on the Quaternary evolution of an alluvial fan system. *Annals of Geophysics*, *46*(October), 775–791. https://doi.org/10.4401/ag-3455

Martínez-Díaz, J. J., Masana, E., & Ortuño, M. (2012). Active tectonics of the Alhama de murcia fault, Betic Cordillera, Spain. *Journal of Iberian Geology*, *38*(1), 253–270. https://doi.org/10.5209/rev_JIGE.2012.v38.n1.39218

Martínez Solares, J. (2003). Sismicidad histórica de la Península Ibérica. *Física de la Tierra*, *15*(15), 13–28. https://doi.org/10.5209/rev_FITE.2003.v15.12634

Masana, E., Martínez-Díaz, J. J., Hernández-Enrile, J. L., & Santanach, P. (2004). The Alhama de Murcia fault (SE Spain), a seismogenic fault in a diffuse plate boundary: Seismotectonic implications for the Ibero-Magrebian region. *Journal of Geophysical Research*, *109*(B1), 1–17. https://doi.org/10.1029/2002JB002359

Masana, E., Moreno, X., Gràcia, E., Pallàs, R., Ortuño, M., López, R., et al. (2018). First evidence of paleoearthquakes along the Carboneras fault zone (SE Iberian Peninsula): Los Trances site. *Geológica Acta*, *16*(4), 461–476. https://doi.org/10.1344/GeologicaActa2018.16.4.8

Masana, E., Pallàs, R., Perea, H., Ortuño, M., Martínez-Díaz, J. J., García-Meléndez, E., & Santanach, P. (2005). Large Holocene morphogenic earthquakes along the Albox fault, Betic Cordillera, Spain. *Journal of Geodynamics*, *40*(2–3), 119–133. https://doi.org/10.1016/j.jog.2005.07.002

Meijninger, B. M. L., & Vissers, R. L. M. (2006). Miocene extensional basin development in the Betic Cordillera, SE Spain revealed through analysis of the Alhama de Murcia and Crevillente Faults. *Basin Research*, *18*(4), 547–571. https://doi.org/10.1111/j.1365-2117.2006.00308.x

Mezcua, J. (1982). *Catálogo general de isosistas de la Península Ibérica*. Instituto Geográfico Nacional.

Montenat, C. (1973). *Les formations neogenes et quaternaires du Levant Espagnol: (provincies d'Alicante et de Murcia)* (Doctoral Dissertation). Université de Paris Sud.

Montenat, C., Ott D'Estevou, P., & Masse, P. (1987). Tectonic-sedimentary characters of the Betic Neogene basins evolving in a crustal transcurrent shear zone (SE Spain). *Bulletin des Centres de Recherches Exploration-Production Elf-Aquitaine*, *11*(1), 1–22.

Murray, A. S., & Wintle, A. G. (2000). Luminescence dating of quartz using an improved single-aliquot regenerative-dose protocol. *Radiation Measurements*, *32*(1), 57–73. https://doi.org/10.1016/S1350-4487(99)00253-X

Murray, A. S., & Wintle, A. G. (2003). The single aliquot regenerative dose protocol: Potential for improvements in reliability. *Radiation Measurements*, *37*(4–5), 377–381. https://doi.org/10.1016/S1350-4487(03)00053-2

Ortuño, M., Masana, E., García-Meléndez, E., Martínez-Díaz, J. J., Štěpančíková, P., Cunha, P. P., et al. (2012). An exceptionally long paleoseismic record of a slow-moving fault: The Alhama de Murcia fault (Eastern Betic shear zone, Spain). *Bulletin of the Geological Society of America*, *124*(9–10), 1474–1494. https://doi.org/10.1130/B30558.1

Ramsey, C. B. (2017). Methods for summarising radiocarbon datasets. *Radiocarbon*, *59*(2), 1809–1833. https://doi.org/10.1017/rdc.2017.108

Reimer, P. J., Austin, W. E. N., Bard, E., Bayliss, A., Blackwell, P. G., Bronk Ramsey, C., et al. (2020). The IntCal20 northern hemisphere radiocarbon age calibration curve (0–55 cal kBP). *Radiocarbon*, *62*(4), 725–757. https://doi.org/10.1017/RDC.2020.41

Ren, J., Xu, X., Yeats, R. S., & Zhang, S. (2013). Latest Quaternary paleoseismology and slip rates of the Longriba fault zone, eastern Tibet: Implications for fault behavior and strain partitioning. *Tectonics*, *32*(2), 216–238. https://doi.org/10.1002/tect.20029

Rivas-Medina, A., Benito, B., & Miguel Gaspar-Escribano, J. (2018). Approach for combining fault and area sources in seismic hazard assessment: Application in south-eastern Spain. *Natural Hazards and Earth System Sciences*, *18*(11), 2809–2823. https://doi.org/10.5194/nhess-18-2809-2018

Serpelloni, E., Vannucci, G., Pondrelli, S., Argnani, A., Casula, G., Anzidei, M., et al. (2007). Kinematics of the Western Africa-Eurasia plate boundary from focal mechanisms and GPS data. *Geophysical Journal International*, *169*(3), 1180–1200. https://doi.org/10.1111/j.1365-246X.2007.03367.x

SHAKE Working Group. (2022). High resolution DTM of the Alhama de Murcia fault and carboneras fault (SE Spain) [Dataset]. SHAKE. http://dx.doi.org/10.6084/m9.figshare.19729597.v1

Sibson, R. H., & Ghisetti, F. C. (2018). Review: Factors affecting the assessment of earthquake hazard from compressional inversion structure. *Bulletin of the Seismological Society of America*, *108*(4), 1819–1836. https://doi.org/10.1785/0120170375

Silva, P. G. (1994). *Evolución geodinámica de la Depresión del Guadalentín desde el Mioceno superior hasta la actualidad: Neotectónica y geomorfología* (Doctoral dissertation). Universidad Complutense de Madrid.

Silva, P. G., Goy, J. L., Somoza, L., Zazo, C., & Bardají, T. (1993). Landscape response to strike-slip faulting linked to collisional settings: Quaternary tectonics and basin formation in the Eastern Betics, southeastern Spain. *Tectonophysics*, *224*(4), 289–303. https://doi.org/10.1016/0040-1951(93)90034-H

Silva, P. G., Goy, J. L., Zazo, C., & Bardají, T. (2003). Fault-generated mountain fronts in southeast Spain: Geomorphologic assessment of tectonic and seismic activity. *Geomorphology*, *50*(1–3), 203–225. https://doi.org/10.1016/S0169-555X(02)00215-5

Silva, P. G., Harvey, A. M., Zazo, C., & Goy, J. L. (1992). Geomorphology, depositional style and morphometric relationships of Quaternary alluvial fans in the Guadalentin Depression (Murcia, southeast Spain). *Zeitschrift Fur Geomorphologie*, *36*(3), 325–341. https://doi.org/10.1127/zfg/36/1992/325

Silva, P. G., Rodríguez-Pascua, M. A., Giner-Robles, J. L., Perez-Lopez, R., Gomez Lario, J., Perucha Atienza, M., et al. (2014). *Catálogo de los efectos geológicos de los terremotos en España* (Vol. 4). Instituto Geológico y Minero de España. Retrieved from http://igmepublicaciones.blogspot.com.es/

Stirling, M., McVerry, G., Gerstenberger, M., Litchfield, N., Van Dissen, R., Berryman, K., et al. (2012). National seismic hazard model for New Zealand: 2010 update. *Bulletin of the Seismological Society of America*, *102*(4), 1514–1542. https://doi.org/10.1785/0120110170

Stuiver, M., & Polach, H. A. (1977). Discussion reporting of 14 C data. *Radiocarbon*, *19*(3), 355–363. https://doi.org/10.1017/S0033822200003672

Sylvester, A. G. (1988). Strike-slip faults. *Geological Society of America*, *100*(11), 1666–1703. https://doi.org/10.1130/0016-7606(1988)100<1666:ssf>2.3.co;2

Valentini, A., Visini, F., & Pace, B. (2017). Integrating faults and past earthquakes into a probabilistic seismic hazard model for peninsular Italy. *Natural Hazards and Earth System Sciences*, *17*(11), 2017–2039. https://doi.org/10.5194/nhess-17-2017-2017

Vergés, J., Marzo, M., & Muñoz, J. A. (2002). Growth strata in foreland settings. *Sedimentary Geology*, *146*(1–2), 1–9. https://doi.org/10.1016/S0037-0738(01)00162-2

Woessner, J., Laurentiu, D., Giardini, D., Crowley, H., Cotton, F., Grünthal, G., et al. (2015). The 2013 European seismic hazard model: Key components and results. *Bulletin of Earthquake Engineering*, *13*(12), 3553–3596. https://doi.org/10.1007/s10518-015-9795-1

Youngs, R. R., & Coppersmith, K. J. (1985). Implications of fault slip rates and earthquake recurrence models to probabilistic seismic hazard estimates. *Bulletin of the Seismological Society of America*, *75*(4), 939–964. https://doi.org/10.1016/0148-9062(86)90651-0

Zechar, J. D., & Frankel, K. L. (2009). Incorporating and reporting uncertainties in fault slip rates. *Journal of Geophysical Research*, *114*(12), 1–9. https://doi.org/10.1029/2009JB006325